The Effects of a Well-Resolved Stratosphere on the Simulated Boreal Winter Circulation in a Climate Model

YOSHIO KAWATANI

Japan Agency for Marine-Earth Science and Technology, Yokohama, Japan

KEVIN HAMILTON

International Pacific Research Center, University of Hawai'i at Mānoa, Honolulu, Hawaii

LESLEY J. GRAY AND SCOTT M. OSPREY

National Centre for Atmospheric Science, Atmospheric, Oceanic and Planetary Physics, Department of Physics, Oxford University, Oxford, United Kingdom

SHINGO WATANABE AND YOUSUKE YAMASHITA

Japan Agency for Marine-Earth Science and Technology, Yokohama, Japan

(Manuscript received 18 July 2018, in final form 7 February 2019)

ABSTRACT

The impact of stratospheric representation is investigated using the Model for Interdisciplinary Research on Climate Atmospheric General Circulation Model (MIROC-AGCM) run with different model-lid heights and stratospheric vertical resolutions, but unchanged horizontal resolutions (~1.125°) and subgrid parameterizations. One-hundred-year integrations of the model were conducted using configurations with 34, 42, 72, and 168 vertical layers and model-lid heights of ~27 km (L34), 47 km (L42), 47 km (L72), and 100 km (L168). Analysis of the results focused on the Northern Hemisphere in winter. Compared with the L42 model, the L34 model produces a poorer simulation of the stratospheric Brewer–Dobson circulation (BDC) in the lower stratosphere, with weaker polar downwelling and accompanying cold-pole and westerly jet biases. The westerly bias extends into the troposphere and even to the surface. The tropospheric westerlies and zone of baroclinic wave activity shift northward; surface pressure has negative (positive) biases in the high (mid-) latitudes, with concomitant precipitation shifts. The L72 and L168 models generate a quasi-biennial oscillation (QBO) while the L34 and 42 models do not. The L168 model includes the mesosphere, and thus resolves the upper branch of the BDC. The L72 model simulates stronger polar downwelling associated with the BDC than does the L42 model. However, experiments with prescribed nudging of the tropical stratospheric winds suggest differences in the QBO representation cannot account for L72 − L42 differences in the climatological polar night jet structure. The results show that the stratospheric vertical resolution and inclusion of the full middle atmosphere significantly affect tropospheric circulations.

1. Introduction

Troposphere–stratosphere coupling processes play an important role in meteorological phenomena on time scales from days to years (e.g., Baldwin and Dunkerton 2001; Kidston et al. 2015). These coupling processes involve not only the direct dynamical coupling between the stratosphere and troposphere but also the influence of chemical processes occurring in the stratosphere, especially in the Southern Hemisphere where ozone destruction in the winter/spring polar stratosphere impacts the troposphere as well as the lower stratosphere. This raises the question of how much the inclusion of a well-resolved middle atmosphere changes weather and climate simulations in numerical models. Studies as early as Boville and Cheng (1988) have investigated the effects of

Denotes content that is immediately available upon publication as open access.

Corresponding author: Yoshio Kawatani, yoskawatani@jamstec.go.jp

DOI: 10.1175/JAS-D-18-0206.1

the stratosphere on representations of tropospheric phenomena within global circulation models. More recently Sassi et al. (2010) discussed simulations using the ''low top'' standard Community Atmosphere Model, version 3.0 (CAM3.0), and the ''high top'' Whole Atmosphere Community Climate Model (WACCM) which was developed as an extension of CAM3.0. They conclude that a poorly resolved stratosphere affects the simulated atmospheric behavior in both the stratosphere and troposphere, including surface pressure fields. Hardiman et al. (2012) investigated the effect of a well-resolved stratosphere on surface climate using high- and low-top versions of the Met Office coupled atmosphere–ocean climate model HadGEM2-CC to compare results for phase 5 of the Coupled Model Intercomparison Project (CMIP5) ''historical'' experiment including external forcing in the high-top model with those obtained using the low-top model, which differed only in the vertical extent and vertical resolution above 15 km. They found that the simulated long-term climatology, variability, and trends in surface temperature and sea ice are rather insensitive to the inclusion of a well-resolved stratosphere. However, the representation of the impacts of atmospheric teleconnections on surface climate, such as responses to El Niño–Southern Oscillation (ENSO), the quasi-biennial oscillation (QBO), and sudden stratospheric warmings (SSWs), is improved in the high-top model. Osprey et al. (2013) investigated stratospheric variability in these same high- and low-top models and found a reduction in the westerly bias in the Northern Hemisphere (NH) polar night jet in the high-top model. The simulated QBO, interannual variations in stratospheric water vapor concentration, and frequency of SSW occurrences were all improved in the high-top model and they concluded that an adequate representation of the stratosphere is necessary to capture important tropical and extratropical variability modes.

Sigmond et al. (2008) examined the atmospheric circulation response to CO_2 doubling in high-top and low-top versions of a global atmospheric model. The physical parameterizations in each version of the model were first tuned to produce the most realistic present-day simulation. They showed that the response of the low-top model to doubled CO_2 is significantly different from that of the high-top model, and that this difference is most clearly attributed to the different setting of topographic gravity wave parameterizations in the two versions rather than the direct effect of the different model-top heights.

Charlton-Perez et al. (2013) used a somewhat different approach to this issue by surveying the stratospheric climate and variability simulations from a large number of different CMIP5 models and then looking among the models for systematic dependence on the height of their top boundaries. They showed that, although the mean stratospheric climate appears insensitive to the model-top height, the low-top models generally have very weak stratospheric variability on daily and interannual time scales. However, the lack of stratospheric variability did not appear to have any impact on the ability of the low-top models to reproduce past stratospheric temperature trends. Of course, there are clear limitations to such an approach as the effects of the different physical parameterizations used in each model cannot be removed (e.g., Manzini et al. 2014).

In this study we investigated the effects of the vertical representation of the middle atmosphere on both stratospheric and tropospheric circulation patterns in global model simulations. Our study used a single global atmospheric model framework [Model for Interdisciplinary Research on Climate Atmospheric General Circulation Model (MIROC-AGCM)] run with four different combinations of model-top heights and vertical resolutions. This allowed a systematic look at the effects of including both the stratosphere and mesosphere and an assessment of the degradation of the model simulation introduced by coarsening the stratospheric vertical resolution. The four simulations were conducted with constant horizontal resolutions, constant tropospheric vertical resolutions, and consistent physical subgrid processes in order to isolate as cleanly as possible the effects of the middle atmosphere on simulated tropospheric circulations. To emphasize, all of the parameters governing subgrid-scale process were the same for each version and not tuned separately for each resolution. It is notable that the fine-vertical-resolution versions of the MIROC-AGCM simulate a fairly realistic tropical stratospheric QBO (Kawatani et al. 2009, 2011, 2014) and the simulated QBO is one feature that is strongly dependent on the stratospheric vertical resolution. Experiments are conducted to examine more specifically the effects of the simulated QBO on other aspects of the model climate.

In this paper, we focus primarily on the December–February (DJF) period when we expect strong troposphere–stratosphere dynamical coupling in the NH. The paper is arranged as follows. Section 2 describes the model and experimental design. Section 3 shows the representation of climatological zonal-mean temperature and zonal wind in the various model configurations. Section 4 presents our analysis of the effects of including the stratosphere on the modeled tropospheric circulation. Section 5 investigates the tropospheric effects of the details of model stratospheric vertical grid including the resolution of the upper stratosphere and mesosphere. Section 6 briefly discusses the effects of enhanced stratospheric representation in the March–May, June–August,

and September–November periods of the year as revealed in our model experiments. Section 7 presents a summary and the conclusions for the study.

2. Model description and experimental design

The model employed is based on the atmospheric component of the MIROC, version 3.2, a coupled atmosphere–ocean GCM (Hasumi and Emori 2004; MIROC-AGCM). The model has a horizontal resolution of T106 spectral truncation, which corresponds to a grid interval of approximately 120 km in the tropics (1.125°). Sensitivity studies were also performed at T213 horizontal resolution (approximately 60 km in the tropics). The MIROC-AGCM used in this study included the mountain-induced gravity wave parameterization by McFarlane (1987), but no nonstationary gravity wave parameterization was included.

Our study is partly concerned with the effects of the imposition of upper boundary conditions at different heights. As is common, the MIROC-AGCM is formulated on a staggered vertical grid in a hybrid sigma–pressure coordinate with vertical velocity defined at half levels and horizontal divergence and vorticity defined at full levels. The upper boundary condition requires zero pressure velocity at a half level formally located at zero pressure. It is known that such a condition effectively acts as an unrealistic reflecting ''lid'' for upward-propagating waves (Lindzen et al. 1968). To reduce unrealistic reflection of vertically propagating waves from the model top, the upper three levels are used as a sponge layer with additional dissipation added to the computed prognostic tendency equations. Specifically the horizontal diffusion is successively doubled (i.e., 2, 4, 8 times) with respect to the standard value in these three uppermost levels. Also in the sponge layer, a linear damping Rayleigh friction is applied to all spectral components of the vorticity and divergence except the zonal-mean (i.e., zonal wavenumber 0) components. The nonzonal Rayleigh friction introduced in the sponge layer by the linear relaxation acts to damp waves without directly affecting the zonal-mean zonal momentum. The potentially very unrealistic effect of artificially damping the zonal-mean momentum are described, for example, in Shepherd et al. (1996). In this paper we will not show results in the sponge layer.

The T106 MIROC-AGCM was run for 100 years in versions with 34, 42, 72, and 168 full levels in the vertical with the highest full level (referred to as the ''model top'') located at ~20 hPa (L34), 1.2 hPa (L42), 1.2 hPa (L72), and 0.000 59 hPa (L168), respectively (corresponding to ~27, 47, 47, and 100 km). Figure 1 shows the vertical-level spacing for each model version. The vertical-level structure from the surface to ~90 hPa is identical in all experiments.

The vertical resolution of the L34 model is the same as that of the L42 model except for its highest layer (layer 34). In the L42 model, the stratospheric vertical-level spacing gradually becomes coarser above 90 hPa, reaching ~2.5 km at 10 hPa. Comparison of L34 and L42 will therefore demonstrate the effect of excluding the middle and/or upper stratosphere.

The L72 model has ~550-m vertical resolution from the upper troposphere to ~5 hPa. The model-top heights of L42 and L72 are the same, but the sponge layers are located slightly differently: above 5.8 hPa for L42 and above 3.6 hPa for L72. Comparison of L42 and L72 will therefore highlight the effect of improved vertical resolution in the stratosphere.

The L168 sponge layer is located above 0.0018 hPa and there is ~550-m vertical resolution up to 0.003 hPa. Comparison of L72 and L168 will therefore highlight the impact of including a well-resolved upper stratosphere and mesosphere.

Note that the computational requirements (in terms of CPU node hours) for the same length of integration of the L42, L72, and L168 versions are 1.5, 4.7, and 13.9 times that of the L34 version, respectively. This comparison is for our model running on the Japan Agency for Marine-Earth Science and Technology (JAMSTEC) Earth Simulator.

To reduce the data amount archived, we processed output data as follows. Monthly mean data were interpolated onto 25 standard pressure levels and results up to 85 hPa for L34 and 10 hPa for L42, L72, and L168 are shown in this study. To investigate tropospheric eddy activity, 6-hourly three-dimensional data up to 70 hPa (interpolated onto 10 pressure levels) were archived. The flux terms in the transformed Eulerian mean (TEM) formulation were internally calculated at each model time step and daily means were output on 34, 42, 72, and 168 pressure levels. The Eliassen–Palm (EP) flux and its divergence were first calculated each day on the full-level structure, and then interpolated onto 25 standard pressure levels for archiving. Note that we will present the EP flux divergence results scaled with mean density so that they represent the contribution of the eddies to the mean flow acceleration ($m\,s^{-1}\,day^{-1}$).

When run with sufficiently fine stratospheric vertical resolution (e.g., ~550 m) the MIROC-AGCM spontaneously simulates a somewhat realistic QBO of the tropical stratosphere. The QBO is simulated in the L72 and L168 models, but not in the L34 and L42 models (the latter display little interannual variability in the tropical stratospheric zonal-mean circulation). It is noteworthy that the QBO can be simulated in this model despite not including a nonstationary gravity wave parameterization (Kawatani et al. 2009, 2011, 2014).

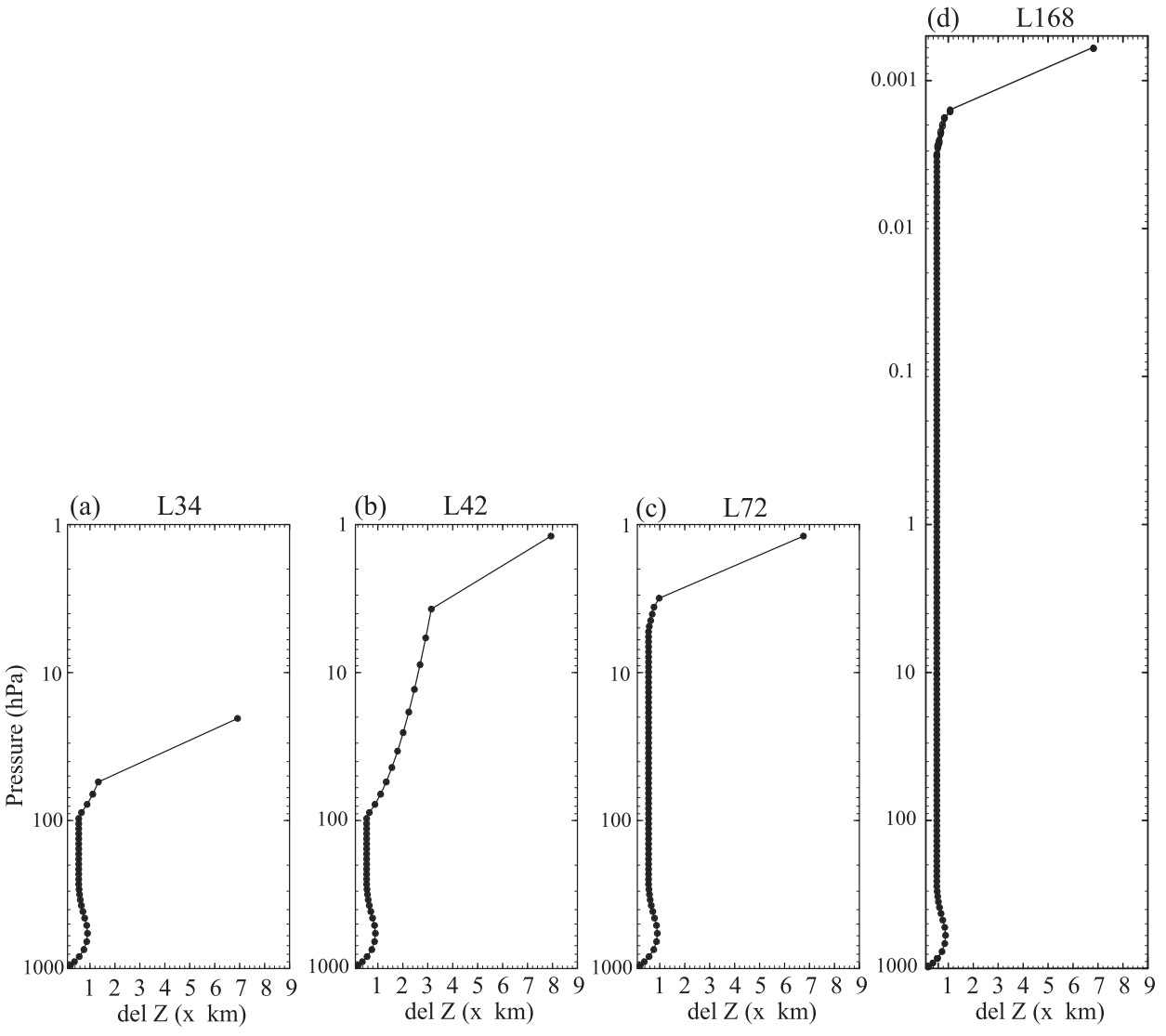

FIG. 1. Vertical-resolution profiles for (a) L34, (b) L42, (c) L72, and (d) L168. Dots show the locations of full grid levels at which the horizontal wind and temperature are computed. The top three levels in each case include strong horizontal diffusion and nonzonal Rayleigh friction to reduce the reflection of vertically propagating waves from the model top (see text for details).

Annually repeating prescribed sea surface temperatures (SSTs) and ozone concentrations were employed. The monthly mean SSTs and sea ice were from the Hadley Centre Sea Ice and Sea Surface Temperature dataset (HadISST) climatology (based on an average from 1979 to 1998). The monthly ozone climatology data were from the U.K. Universities' Global Atmospheric Modelling Programme (UGAMP) monthly ozone climatology dataset (Li and Shine 1999). The UGAMP ozone climatology is based on observations during 1985–89.

Globally and vertically uniform concentrations are prescribed for the radiatively active gases O_2 (21%), CO_2 (345 ppmv), CH_4 (1.7 ppmv), and N_2O (0.3 ppmv). The CO_2 concentration prescribed here is close to the NOAA Global Greenhouse Gas Network (GGGN) estimate of the annual-mean, global-mean mixing ratio for 1985 (ftp://aftp.cmdl.noaa.gov/products/trends/co2/co2_annmean_gl.txt). The 1.7-ppmv CH_4 concentration specified in our model is close to the GGGN estimate of the annual-mean, global-mean mixing ratio for 1989. The 0.3 ppmv adopted for N_2O also agrees with published observational estimates circa 1980 (e.g., https://www.epa.gov/sites/production/files/2016-08/documents/print_ghg-concentrations-2016.pdf). The water vapor concentrations throughout the atmosphere are computed prognostically including a middle-atmospheric source via a parameterization of methane oxidation [see Kawatani et al. (2014) for details]. Other aspects of

the model formulation are described in Kawatani et al. (2011).

To summarize, in these experiments (i) there is no interannual variability of external forcing, (ii) the annually repeating prescribed SSTs are computed as the mean over the base period 1979–98, and (iii) the prescribed concentrations of radiatively active gases are reasonably representative of conditions during that base period as well. The model climatology will be compared with atmospheric observations averaged over 1979–98.

3. Representation of climatological zonal-mean temperature and zonal wind

Figures 2 and 3 show climatological DJF- and zonal-mean temperature and zonal wind for each model, together with ERA-Interim (hereafter ERA-I; Dee et al. 2011) data averaged from 1979 to 1998. Results of T213L168 are also included here, but this version was integrated for only 35 years due to limited computational resources. Only areas with differences judged to be nonzero with statistical confidence of ≥95% are shaded. The statistical significance is based on the two-sided Student's t test for sampling the 100 (T106), 35 (T213), and 20 (ERA-I) individual DJF-mean data points (effectively considering each DJF period as independent). The cold bias in the NH polar region and westerly bias in the polar night jet become less severe with increasing vertical resolution and with a higher model top, but statistically significant cold and westerly biases are still found even in the T106L168 model simulation. These models did not include any nonstationary gravity wave parameterization; experience with other global models (e.g., Hamilton et al. 1999) suggests that the westward force exerted by gravity wave momentum deposition in the polar night upper stratosphere and mesosphere explicitly represented by a T106 model would be underestimated and that biases would be reduced in a higher-horizontal-resolution version.

This issue was investigated here by running a T213L168 version of the MIROC-AGCM. Although different parameters are usually used in T106 and T213 model runs, we used the same parameters in the T213L168 model to isolate the effects of horizontal resolution. Results are shown in Figs. 2b and 3b. As expected, the cold-pole and westerly jet biases are improved at finer horizontal resolution. The T213L168 simulation of the polar night jet is actually slightly weaker around 50 hPa and 60°N than indicated by the ERA-I data. We focus on results from T106 models from now on, as the main purpose of this study is to investigate the effects of the vertical representation of the stratosphere on tropospheric phenomena.

Unlike the stratospheric mean wind and temperature biases, the tropospheric biases in Figs. 2 and 3 are not dramatically improved by simply increasing the model-top height and stratospheric vertical resolution. Nevertheless, the L34 model results do feature larger cold biases around both the North and South Poles at 100–200 hPa, and a warm bias at ~45°N, together with concomitant westerly wind biases. Obviously biases in the simulated mean climatology may be associated with biases in simulated variability.

4. The effects of the stratosphere on tropospheric circulations

In this section, we discuss the effects of the stratosphere on the simulation of tropospheric circulations by comparing results from the L34 and L42 models. The focus is on regions where the differences in the DJF-mean climatology between models are judged to be nonzero with statistical confidence greater than 95%. Hereafter, differences revealed by subtracting the L42 model results from the L34 results are referred to as "L34 − L42."

Figure 4 shows latitude–height cross sections of zonal-mean temperature and zonal wind differences, together with L34 climatological values. Difference fields are shown only up to 85 hPa because the L34 model has only the sponge layer above this level (see Fig. 1). Large negative differences (i.e., lower temperatures in L34) are seen in high latitudes and positive differences are found in lower latitudes. Consistent with thermal wind balance, the L34 westerlies are stronger (weaker) in the higher (lower) latitudes. In the NH, the L34 stratospheric polar night jet is stronger around 60°N and 100 hPa, and the westerly wind differences extend down to the surface. In the Southern Hemisphere (SH), the results indicate a poleward shift of the subtropical jet in L34 relative to L42.

Purple and green lines in Fig. 4a show the tropopause height (World Meteorological Organization definition) in the L34 and L42 models, respectively. The stratospheric absorption of solar shortwave radiation may be reduced in L34 versus L42 and hence more solar radiation reaches tropopause levels, contributing somewhat to the positive L34 − L42 temperature differences in the subtropical and tropical regions.

Figure 5a shows the L42 latitude–height cross sections of zonal-mean zonal wind and residual-mean vertical velocity $\overline{w}^*$ in the TEM formulation. As expected, the large-scale stratospheric meridional circulation [Brewer–Dobson circulation (BDC)] revealed here is characterized by upwelling in the tropics and downwelling in the high latitudes.

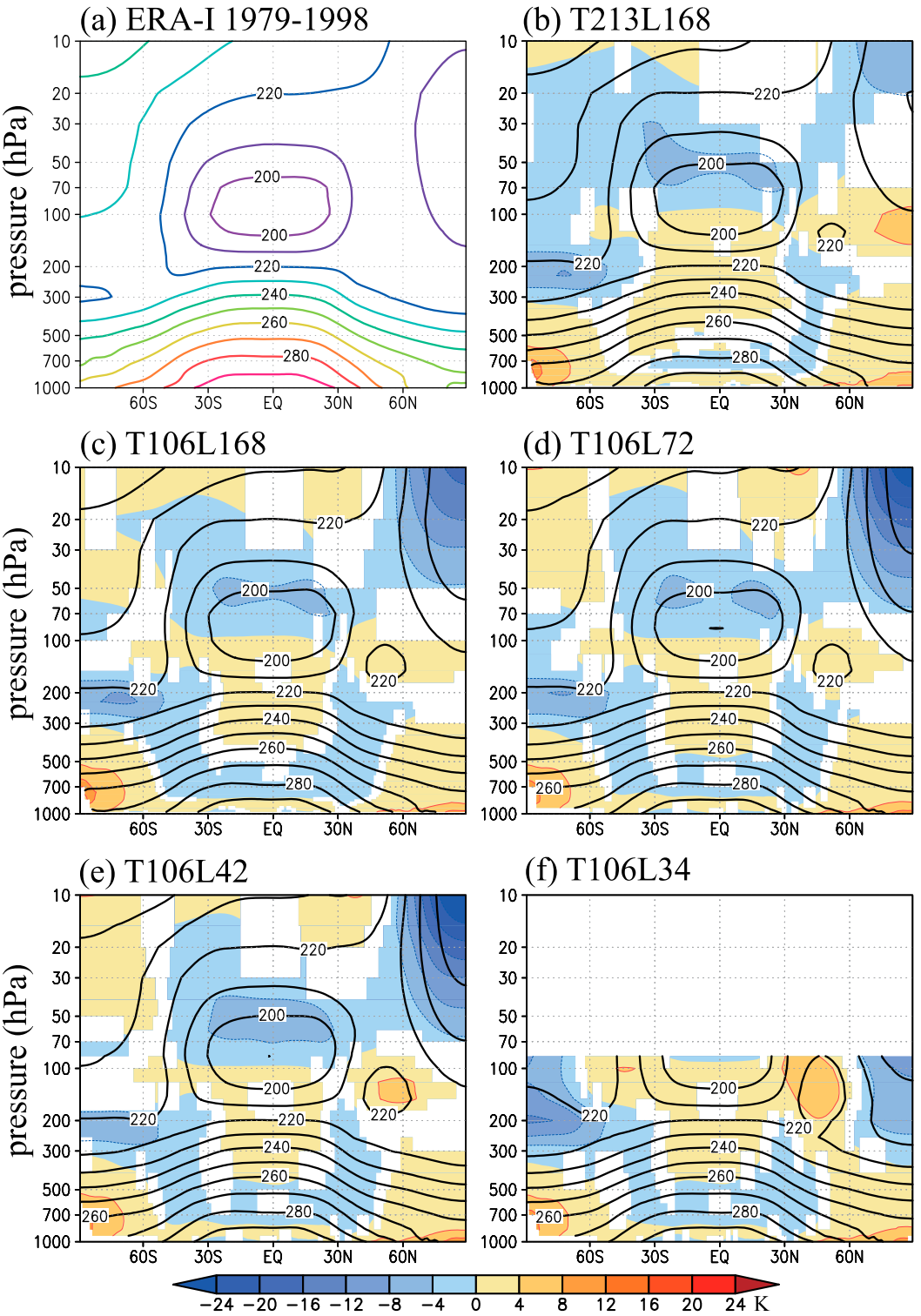

FIG. 2. Climatological DJF zonal-mean temperatures (contours) for (a) ERA-I, (b) T213L168, (c) T106L168, (d) T106L72, (e) T106L42, and (f) T106L34. Color shading indicates the model minus ERA-I temperature and is plotted only when the difference has a statistical confidence ≥95% for the model minus ERA-I. The contour and color intervals are 10 and 4 K, respectively.

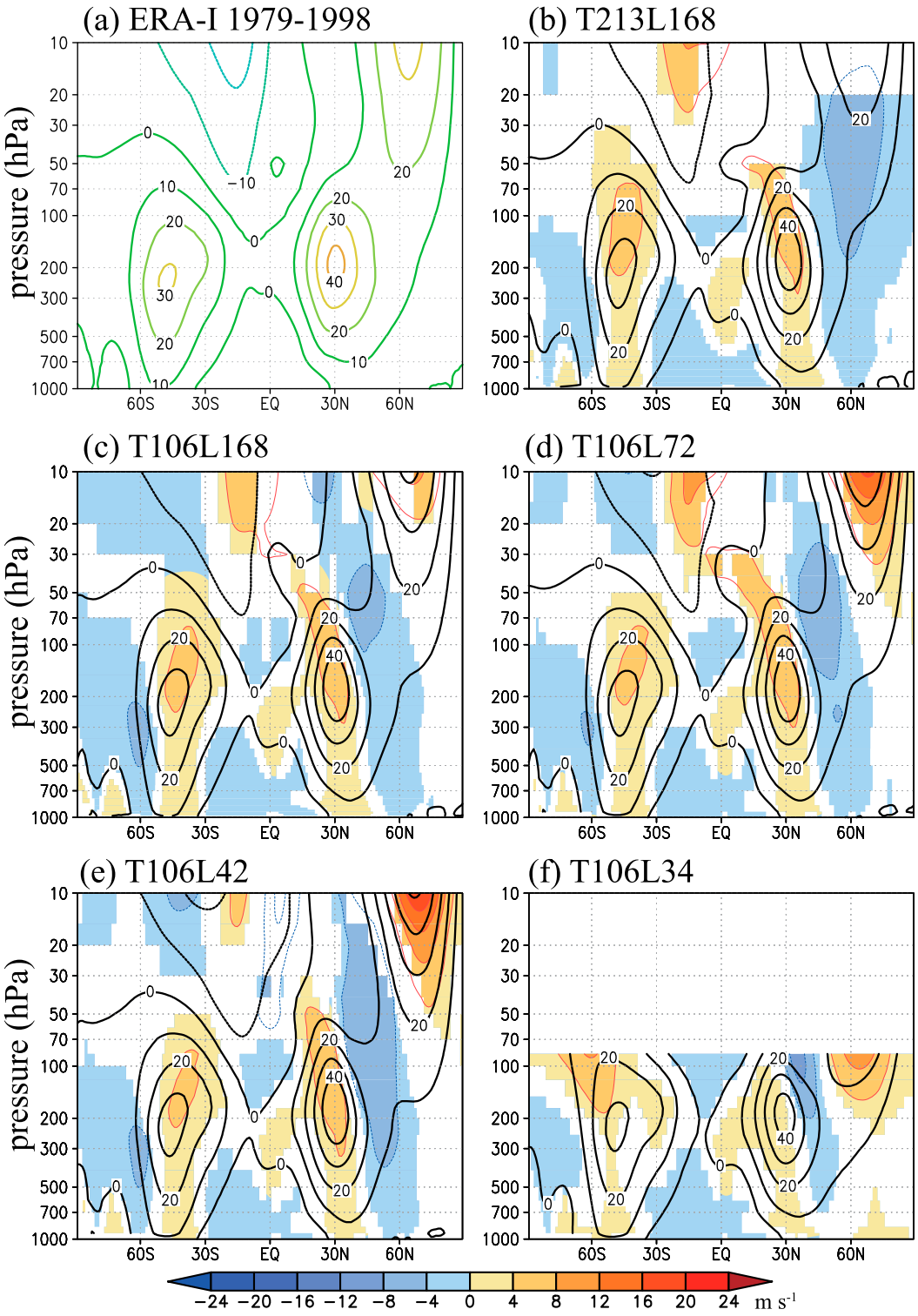

FIG. 3. As in Fig. 2, but for zonal-mean zonal wind. The contour and color intervals are 10 and 4 m s^{-1}, respectively.

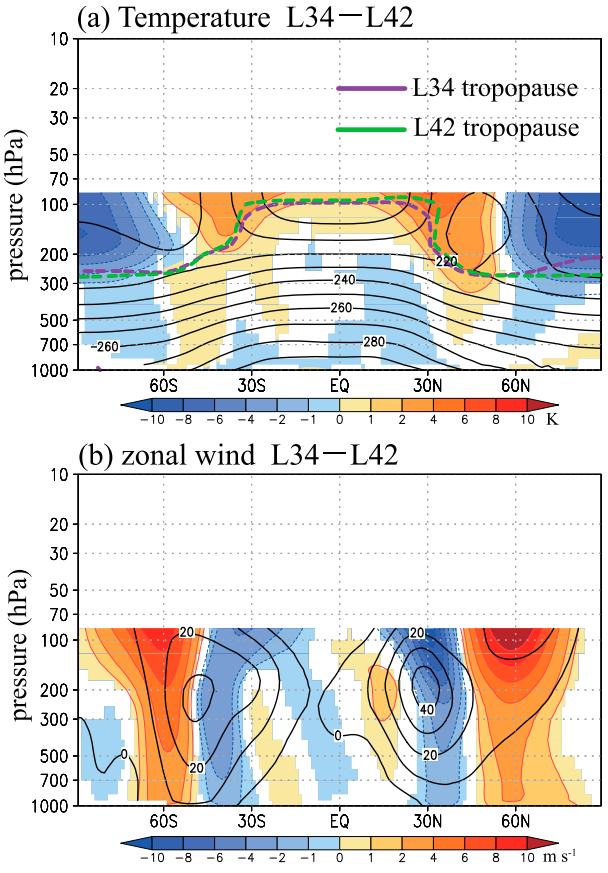

FIG. 4. Latitude–height cross sections of the L34 − L42 differences in climatological DJF zonal-mean (a) temperature and (b) zonal wind. Color shading indicates differences with a statistical confidence ≥95%. Black contours show the L34 zonal-mean temperature and zonal wind at intervals of 10 K and 10 m s^{-1}, respectively. The color shading is at ±1, ±2, ±4, ±6, ±8, and ±10 K for (a) and ±1, ±2, ±4, ±6, ±8, and ±10 m s^{-1} for (b). The tropopause, as defined by the World Meteorological Organization, is denoted by purple (L34) and green (L42) dashed lines.

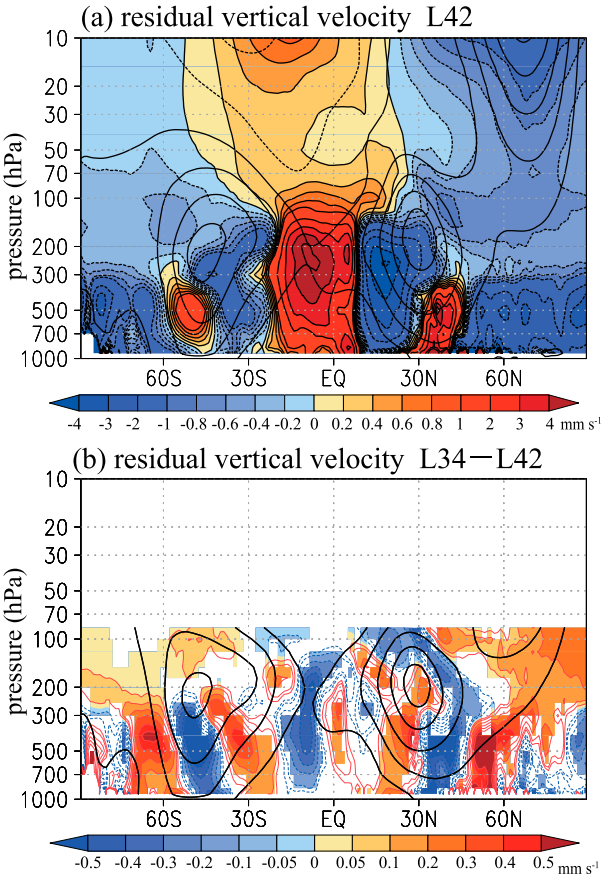

FIG. 5. Latitude–height cross sections of (a) the climatological DJF-mean residual-mean vertical velocity (color shading) in the L42 model and (b) the L34 − L42 difference in this quantity. In (b) the color shading indicates values with a statistical confidence ≥95%. The black contour lines show the zonal-mean zonal wind in the (a) L42 and (b) L34 models with contour intervals of 10 m s^{-1}. The color shading is at ±0.2, ±0.4, ±0.6, ±0.8, ±1, ±2, ±3, and ±4 mm s^{-1} for (a) and ±0.05, ±0.1, ±0.2, ±0.3, ±0.4 and ±0.5 mm s^{-1} for (b).

Figure 5b shows L34 − L42 $\overline{w}^*$ differences. Significant large positive differences are seen in the mid- to high latitudes, indicating weaker BDC downwelling in the L34 model than in the L42 model. A compensating effect is seen in the difference fields at low latitudes, consistent with an overall weaker BDC in the L34 model.

The BDC is mainly driven by atmospheric waves, such as planetary and gravity waves, that propagate from the troposphere into the stratosphere and dissipate in the extratropical and subtropical stratosphere. This wave dissipation results in westward wave forcing of the mean flow in the extratropical stratosphere and generates poleward flow in the midlatitudes and upwelling in the tropics (e.g., Butchart 2014). There are only three vertical levels above 100 hPa (i.e., 97, 88, and 78 hPa, excluding the top three sponge levels; see Fig. 1a) in the L34 model. We may expect that most of the stratospheric westward forcing presumably is not present in the L34 model, due to poor representation of wave–mean flow interaction above ~80 hPa, and the simulated BDC is consequently underestimated in the lower stratosphere and the upper troposphere.

The upper boundary itself may also have a fairly direct effect on the BDC. Although the zero mass flux (pressure velocity) condition is imposed nominally at zero pressure, the first nonzero vertical velocities will be computed for the model half level below the top full level and the "lid" condition may be expected to suppress this highest-level vertical velocity to some extent. The lack of any representation of the dynamics above ~27 km in the L34 model may be expected to significantly suppress the BDC

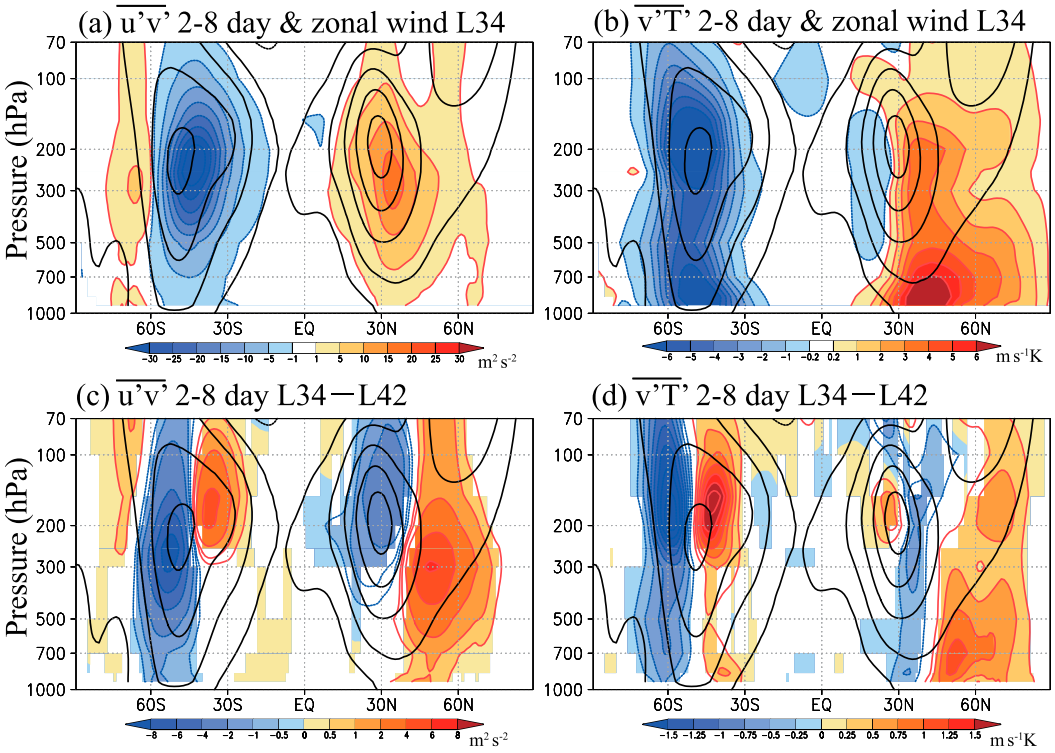

FIG. 6. (top) Latitude–height cross sections of the DJF-mean L34 model zonal-mean (a) meridional flux of zonal momentum $\overline{u'v'}$ and (b) meridional heat flux $\overline{v'T'}$ associated with eddies with periods from 2 to 8 days. (bottom) The L34 − L42 differences for (c) $\overline{u'v'}$ and (d) $\overline{v'T'}$. Black contours represent zonal-mean zonal winds from the L34 model with contour intervals of 10 m s^{-1}. Color shading is at ±1, ±5, ±10, ±15, ±20, ±25, and ±30 m^2 s^{-2} for (a); ±0.2, ±1, ±2, ±3, ±4, ±5, and ±6 m s^{-1} K for (b); and ±0.5, ±1, ±2, ±4, ±6, and ±8 m^2 s^{-2} for (c); and color interval is 0.25 m s^{-1} K for (d). Values with a statistical confidence of ≥95% are colored in (c) and (d).

and reduce polar downwelling. The weak high-latitude downwelling in L34 results in weaker adiabatic heating, which corresponds to colder mean temperatures in the polar regions (Fig. 4a). Overall the absence of much of the stratospheric dynamics from the L34 model may be expected to result in a mean temperature unrealistically close to radiative equilibrium.

Figures 6a and 6b show the L34 results for the latitude–height cross sections of the climatological DJF-mean zonal-mean meridional flux of zonal momentum $\overline{u'v'}$ and heat $\overline{v'T'}$ contributed by eddies with periods from 2 to 8 days (i.e., the eddy fluxes associated with synoptic-scale disturbances). The black contours represent the zonal-mean zonal wind. Positive and negative $\overline{u'v'}$ and $\overline{v'T'}$ values are seen near the subtropical jets in the NH and SH respectively, indicating poleward transport of momentum and heat by the synoptic eddies.

The L34 − L42 $\overline{u'v'}$ and $\overline{v'T'}$ differences are shown in Figs. 6c and 6d. Significant positive $\overline{u'v'}$ differences are seen north of ~40°N and negative differences are found around the subtropical jet in the SH. Eddy heat flux differences are also positive (negative) in the higher latitudes in the NH (SH), indicating poleward shifts in the baroclinic wave activity in the L34 model. The differences for $\overline{u'v'}$ and $\overline{v'T'}$ with all eddies included (not shown) have nearly identical patterns as the synoptic contributions shown in Fig. 6. The poleward shift in $\overline{u'v'}$ in L34 corresponds well to the shift in the westerly jets as seen in the zonal wind differences (Fig. 4b).

Figure 7a is a map of the DJF-mean 850-hPa L34 − L42 zonal wind differences; the black contours indicate the L34 climatological DJF mean. As seen in Fig. 4b, the 850-hPa zonal wind pattern shifts poleward in the L34 model compared with that in the L42 model, but there are some differences between the NH and SH. In the SH, this difference field is nearly zonally uniform, with negative values around 40°S and positive values around 60°S. On the other hand, the differences in the NH are less zonally uniform. Significant differences are seen extending southwest to northeast in the Atlantic; they are locally large in the central to eastern Pacific and small in the eastern and western Pacific where they display more complicated structures. Fig. 7b shows the L34 − L42 meridional eddy heat flux $\overline{v'T'}$ difference together with L34 climatology. Eddy heat fluxes are shifted poleward in the L34 model compared with those

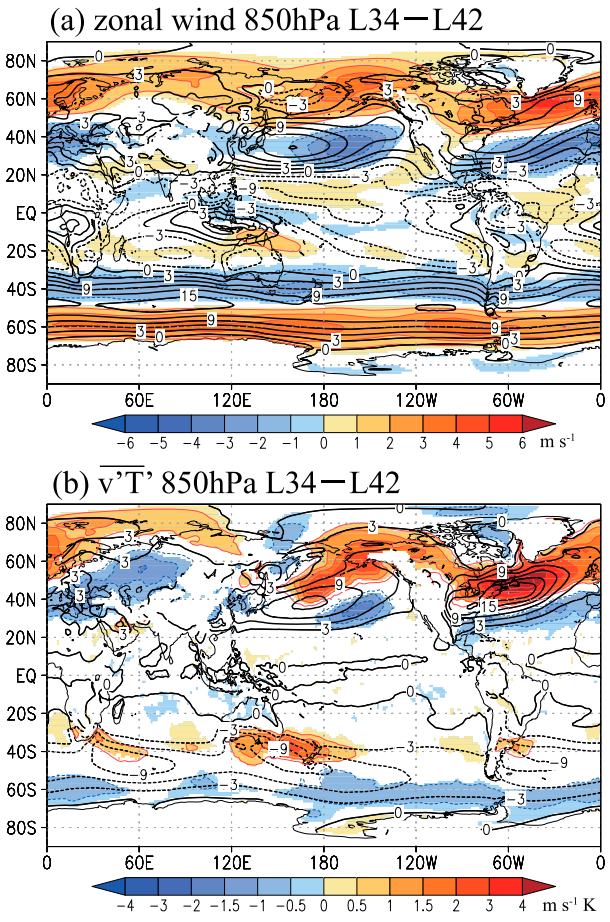

FIG. 7. Horizontal map of the L34 − L42 differences in climatological DJF (a) zonal wind and (b) eddy heat flux $\overline{v'T'}$ at 850 hPa. Black contour lines indicate the climatological-mean (a) zonal wind and (b) $\overline{v'T'}$ from the L34 model. Color interval is 1 m s^{-1} for (a), and color shading is at ±0.5, ±1, ±1.5, ±2, ±3, and ±4 m s^{-1} K for (b). Values with a statistical confidence ≥95% are colored. Black contour intervals are 3 m s^{-1} for (a) and 3 m s^{-1} K for (b).

in the L42 model, as seen in the zonal-mean field (Fig. 6d), but also display some more local structures, especially in the NH.

Figure 8 shows horizontal maps of 2-m atmospheric temperature [surface air temperature (SAT)], sea level pressure (SLP), and precipitation differences for L34 − L42. Note that positive precipitation differences are indicated by red colors, using the same convention as for other quantities. The black contours in Figs. 8b and 8c show the climatological DJF-mean SLP and precipitation in the L34 model. The SAT L34 − L42 differences are generally smaller over ocean areas than over land—an understandable consequence of using the same imposed SSTs in both model versions. The L34 − L42 SAT difference map resembles the positive-phase Arctic Oscillation (AO+) structure. Specifically, the field in Fig. 8a shows warm conditions over Europe and cool conditions

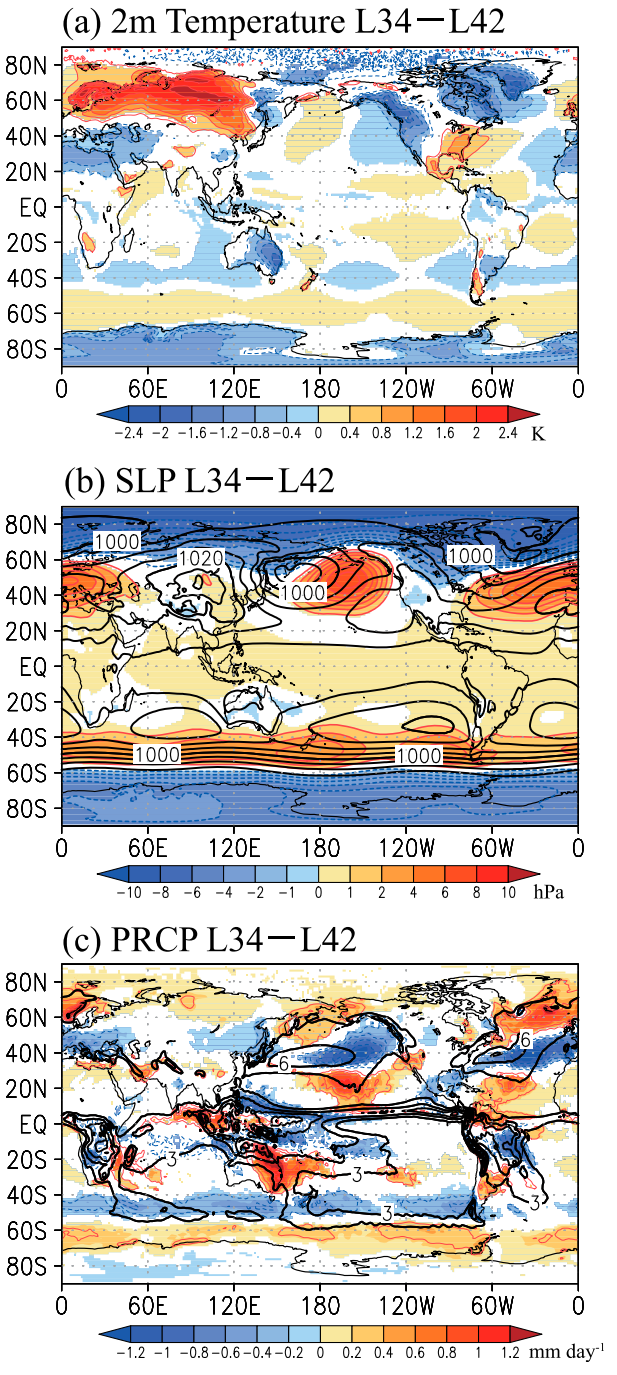

FIG. 8. Horizontal maps of the L34 − L42 differences in DJF climatological-mean (a) 2-m air temperature, (b) sea level pressure (SLP), and (c) precipitation. The black contour lines in (b) and (c) are the climatological means of L34 SLP and precipitation. The color interval is 0.4 K for (a), the color shading is at ±1, ±2, ±4, ±6, ±8, and ±10 hPa for (b), and the color interval is 0.2 mm day^{-1} for (c). Values with a statistical confidence ≥95% are colored. Black contour intervals are 5 hPa for (b) and 3 mm day^{-1} for (c).

in the northeastern areas of North America and Greenland, characteristic of the AO+ pattern (although note that the negative values over western North America in the L34 − 42 SAT difference map deviate from the usual AO+ pattern). This overall AO+ pattern is consistent with what is seen in the real atmosphere when the polar night jet is stronger than usual, and so it is reasonable that this difference in SAT accompanies the L34 − L42 model jet differences (Fig. 4b).

Corresponding to the distribution of the zonal wind anomalies (Figs. 4b, 7a), the SLP differences are generally negative in the polar region and positive in the midlatitudes, indicating that the L34 model simulates generally lower (higher) SLP in the polar (midlatitude) region (Fig. 8b). Like the 2-m temperature anomalies, the SLP anomalies are more zonally uniform in the SH and more locally distributed in the NH. In the central Pacific, around 40°–60°N, locally large positive SLP anomalies are observed. Compared with the ERA-I SLP data, the core of the Aleutian low shifts westward in L34 and has a more realistic location in L42, indicating that inclusion of the stratosphere improves the representation of the Aleutian low, at least for the MIROC-AGCM. The SLP anomalies in the Pacific correspond to the 850-hPa zonal wind differences (Fig. 7a), which are large and somewhat confined in the central Pacific.

In general, the distributions of the precipitation anomalies (Fig. 8c) correspond well to those of the SLP (Fig. 8b) and 850-hPa $\overline{v'T'}$ anomalies (Fig. 7b) poleward of 30°N and 40°S; more precipitation is induced under lower pressure and stronger synoptic eddies, and less precipitation is seen under higher pressure and weaker eddies. This correspondence is much clearer in the SH. Interestingly, significant precipitation anomalies are also observed in the equatorial region. Stratospheric processes, such as sudden stratospheric warming and/or the QBO in tropical circulation, can influence tropical precipitation (Kodera et al. 2015; Liess and Geller 2012; Yoo and Son 2016; Gray et al. 2018). Differences in equatorial precipitation between the L34 and L42 models might be related to the simulation of the BDC, vertical zonal wind shear, tropical tropopause temperature, etc. A detailed investigation is beyond the scope of this study, but should be included in future research.

Figure 9a shows the climatological DJF-mean SLP for the L34 (red contours) and L42 (blue contours) models. As mentioned above, the core of the Aleutian low in L34 is shifted westward ~10° compared with that in L42. Figure 9b illustrates the 500-hPa geopotential height L34 − L42 difference. Negative differences are seen near 20°N, 170°W and to the north of negative precipitation anomalies in the central Pacific, near 5°N (Fig. 8c). Positive differences seen to the north of these

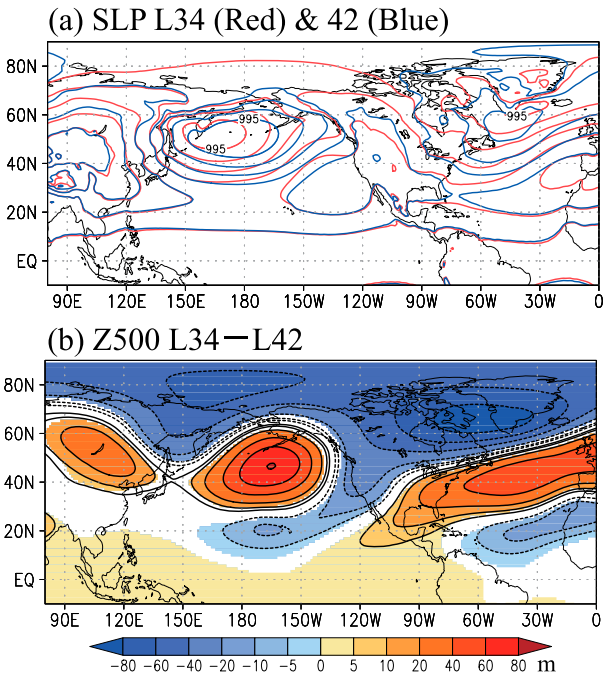

FIG. 9. Horizontal maps of the climatological DJF-mean SLP from L34 (red) and L42 (blue) and (b) the L34 − L42 difference in DJF climatological-mean geopotential height at 500 hPa. The color shading is at ±5, ±10, ±20, ±60, and ±80 m, and values with a statistical confidence ≥95% are colored in (b).

negative anomalies correspond to the positive SLP differences near 40°N (Fig. 8b). These patterns are similar to the negative Pacific–North America (PNA) pattern, which includes negative anomalies over North America and positive anomalies over the southeastern United States (e.g., Wallace and Gutzler 1981).

Figure 10 is a schematic illustrating the differences between the model version without most of the stratosphere (L34) and the version including a representation of the stratosphere (L42): that is, L34 − L42. The effects of the stratosphere on tropospheric circulations in the MIROC-AGCM can be summarized as follows:

1) The L34 model simulates a weaker BDC than does the L42 model, likely due in part to the direct effect of the low model top in suppressing vertical mass fluxes and in part to the absence of wave driving of the mean flow above the model top. Significant residual-mean vertical velocity differences between the models extend from the stratosphere into the troposphere down to about 300–500 hPa at high latitudes.
2) The mean polar temperature is closer to the radiative equilibrium in L34 than in L42 due to the suppression of the BDC and the weaker adiabatic heating associated with the reduced polar downwelling in the L34 model.

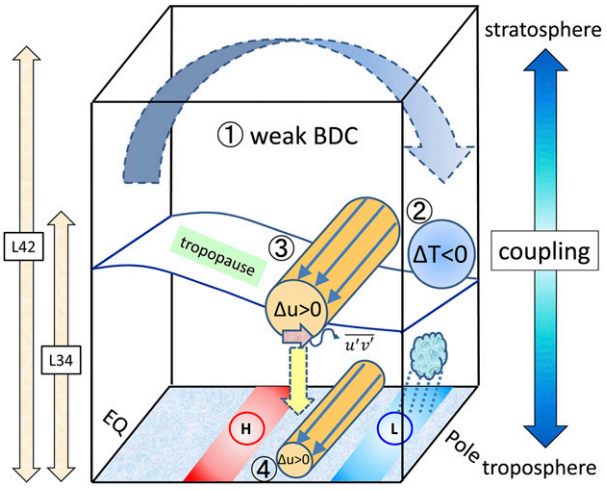

FIG. 10. Schematic illustration of some differences in the simulated circulation between the model without the stratosphere (L34) and the model with the stratosphere (L42); i.e., L34 − L42. Derived in part from the illustration in box 1 of Kidston et al. (2015).

3) The stratospheric jet is stronger, consistent with thermal wind balance.
4) The westerly mean wind differences seen prominently in the stratosphere extend, to some extent, down to the surface. The transport of angular momentum by the waves in the upper troposphere $\overline{u'v'}$ is shifted poleward in L34 relative to L42, a change that mirrors the shift in the mean jet.
5) The distributions of surface pressure and precipitation in the model simulations are also affected by the inclusion of the stratosphere.

5. Effects of stratospheric vertical resolution and inclusion of the upper stratosphere and mesosphere on tropospheric circulations

In this section, we discuss 1) the effects of the stratospheric vertical resolution on tropospheric circulations by comparing the L42 and L72 models and 2) the effects of moving the model top from the upper stratosphere to the upper mesosphere by comparing the L72 and L168 models. Comparing L42 with L168 reveals the combined effects of 1 and 2.

Figure 11 shows latitude–height cross sections of the zonal-mean temperature, zonal wind, and residual-mean vertical velocity $\overline{w}^*$ differences for L42 − L72, L72 − L168, and L42 − L168. Contour lines show climatological temperature and zonal winds for L42 (left), L72 (middle), and L42 (right). In L42 − L72, the statistically significant large easterly differences in the equatorial stratosphere (Fig. 11d) are due to the absence of the QBO in the L42 model; the stratospheric vertical resolution in the L42 model is ~1–3 km (Fig. 1), which is not sufficient to simulate the QBO in the MIROC-AGCM (at least in the absence of nonstationary gravity wave parameterization). In addition, the absence of the QBO in the L42 model (as well as the accompanying QBO secondary circulation; e.g., Plumb and Bell 1982) leads to a tropically confined signal in the L42 − L72 differences in temperature (Fig. 11a) and mean vertical velocity (Fig. 11g). There are significant $\overline{w}^*$ differences in the NH polar stratosphere, indicating weaker downwelling in L42 than in L72 (Fig. 11g). Negative temperature differences appear in the NH polar stratosphere (Fig. 11a), although they are not statistically significant. Statistically significant positive temperature differences are seen near 60°N in the midlatitude lower stratosphere ~200–100 hPa. Easterly and westerly mean wind differences corresponding to these temperature differences are found to the south and north of ~60°N, respectively. The easterly differences around 50°N extend down to the lower troposphere.

In L72 − L168, significant and large positive $\overline{w}^*$ differences (Fig. 11h) are seen in the high-latitude NH stratosphere, indicating weaker downwelling in the L72 model. The L72 − L168 residual-mean vertical velocity differences are negative in the SH high latitudes. The L72 model, which has a fine vertical resolution only up to 5 hPa (Fig. 1), cannot adequately represent the upper branch of the BDC, while the L168 model can resolve the full BDC structure, including in the uppermost stratosphere. This may cause the weaker downwelling in the high latitudes in L72, resulting in colder polar temperatures (Fig. 11b) and a stronger polar night jet (Fig. 11e). The QBO simulation is slightly different in the L72 and L168 models, resulting in difference fields in the equatorial stratosphere in Figures 11b, 11e, and 11h. Figures 11c, 11f, and 11i present the L42 − L168 differences showing the combined effects of improving stratospheric resolution and moving the model top to the upper mesosphere.

The position of the polar night jet core at 10 hPa is located farther south and the meridional extent of the jet is wider in the L42, L72, and L168 model versions successively (see 10 m s^{-1} lines at 10 hPa in Fig. 3). The polar night jet in the L168 model is most similar to that in the ERA-I data. Previous studies have shown that adopting finer model resolution generally acts to improve the polar night jet structure (Hamilton et al. 1999; Watanabe et al. 2008). Under higher vertical resolution and a higher model top, dynamical processes such as wave–mean flow interactions and residual circulations are better represented, which shifts the temperature structure away from radiative equilibrium and toward more realistic values.

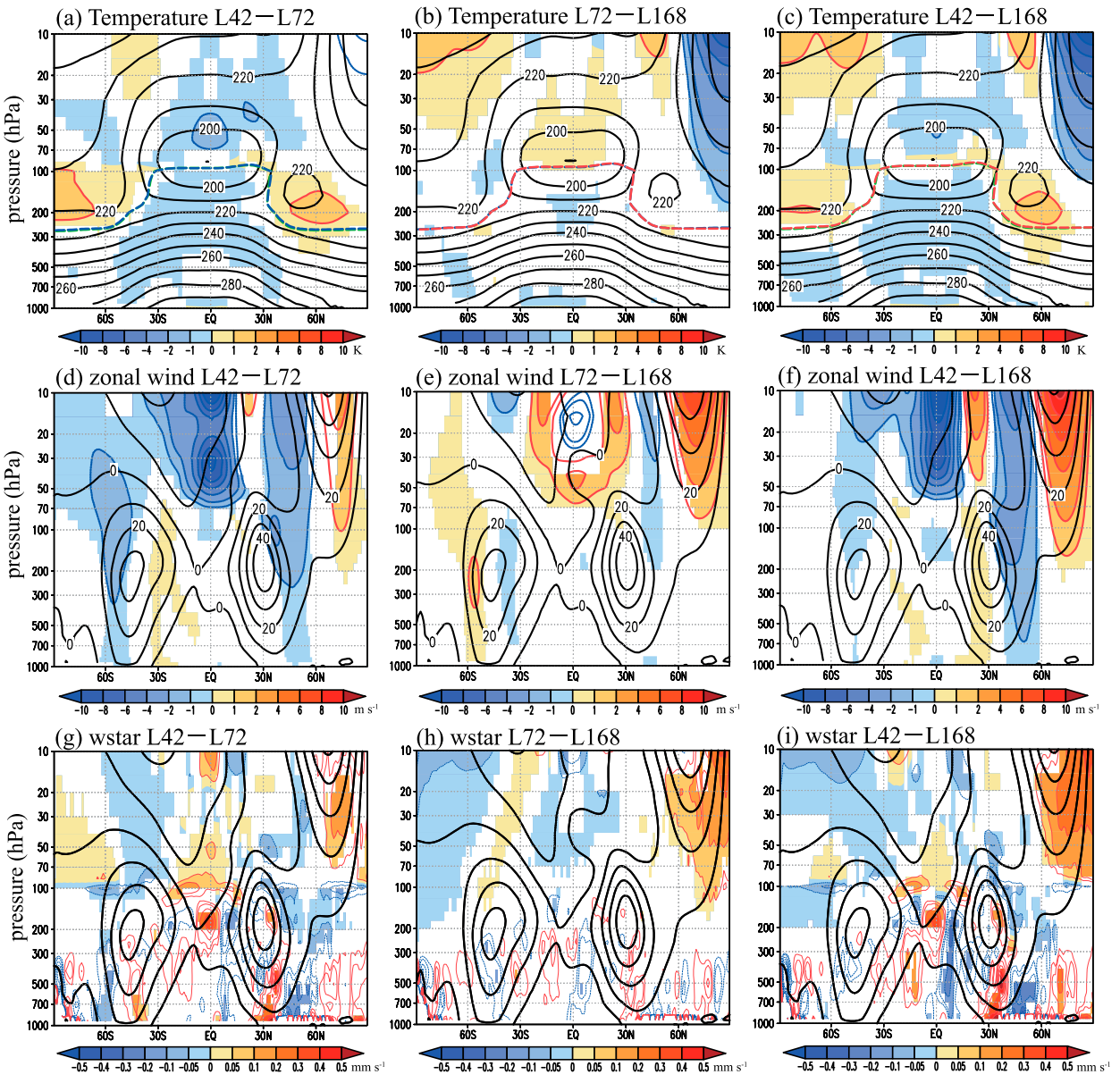

FIG. 11. Latitude–height cross sections of the climatological DJF-mean (a)–(c) zonal-mean temperature, (d)–(f) zonal-mean zonal wind, and (g)–(i) residual-mean vertical velocity differences for (left) L42 − L72, (center) L72 − L168, and (right) L42 − 168. Contour lines show climatological (a)–(c) temperature and (d)–(i) zonal wind in (left) L42, (center) L72, and (right) L42. The dashed lines in (a)–(c) shows tropopause heights for L42 (green), L72 (blue), and L168 (red), which are nearly identical. The color shading is at ±1, ±2, ±4, ±6, ±8, and ±10 K for (a)–(c); ±1, ±2, ±4, ±6, ±8, and ±10 m s^{-1} for (d)–(f); and ±0.05, ±0.1, ±0.2, ±0.3, and ±0.5 mm s^{-1} for (g)–(i). Values with a statistical confidence ≥95% are colored. Black contour intervals are 10 K for (a)–(c) and 10 m s^{-1} for (d)–(i).

Easterly and westerly differences are apparent near 50° and 75°N, respectively, in both L42 − L72 and L72 − L168, reflecting somewhat different simulations of the mean stratospheric polar night jet structure. As seen in the L34 − L42 results, these easterly and westerly differences extend down to into the troposphere; this pattern is especially distinct in the L42–L168 comparison (Fig. 11f). The finer vertical resolution in the stratosphere (L42 − L72) is of greater importance than the inclusion of a mesosphere (L72 − L168) in terms of the impact on the troposphere. This is consistent with Haynes et al. (1991) who suggest that eddy forcing just up to ~50 km will drive at least 80% of the residual vertical velocity at 18 km.

Figure 12a shows latitude–height cross sections for the climatological DJF-mean EP flux and EP flux divergence

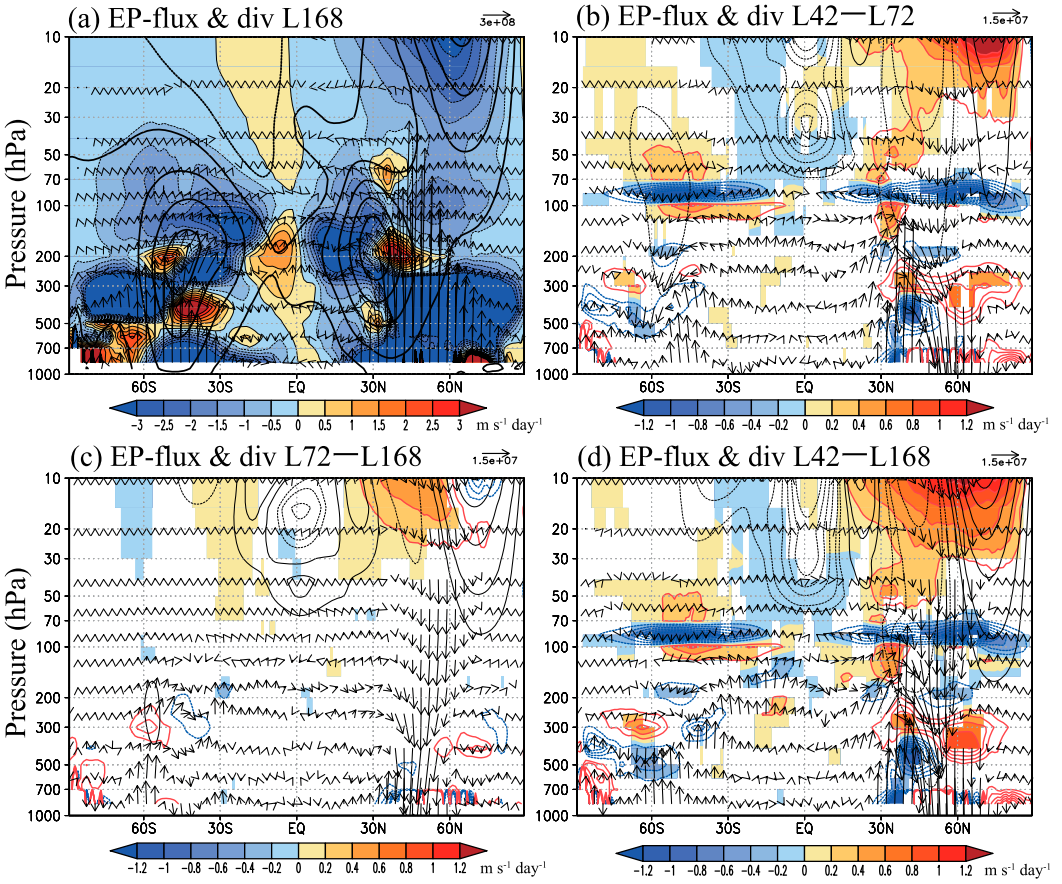

FIG. 12. (a) Latitude–height cross sections of the climatological DJF-mean EP flux (vectors) and EP flux divergence (color shading) in the L168 model. Color intervals are 0.5 m s^{-1} day^{-1}. Zonal-mean zonal winds (contours) are at intervals of 10 m s^{-1}. Also shown are EP flux and EP flux divergence differences for (b) L42 − L72, (c) L72 − L168, and (d) L42 − L168. Differences with a statistical confidence ≥95% are colored. The black contour lines are the climatological zonal-mean zonal wind differences at values of ±1, ±2, ±4, ±6, ±8, and ±10 m s^{-1}. The vertical components of the EP flux are multiplied by a factor of 660. Color intervals are 0.2 m s^{-1} day^{-1}.

in the L168 model. EP flux convergence (i.e., westward mean-flow forcing) is seen in most of the extratropical stratosphere and contributes to the generation of the BDC (Haynes et al. 1991). Figures 12b–d show differences in EP flux and EP flux divergence. The L42 − L72 differences in the EP flux divergence are largely positive in the mid- to high latitudes above ~50 hPa in the NH (Fig. 12b). This result indicates that the westward wave forcing is larger in L72 than in L42. The finer vertical-level spacing in L72 allows this version to resolve more waves with short vertical wavelengths and so possibly to represent more realistic wave–mean flow interactions. Stronger westward forcing induces larger downwelling associated with the BDC in the high-latitude stratosphere (Fig. 11g). Directions of EP flux difference vectors in the NH extratropics correspond to zonal wind differences: downward and upward vectors correspond to regions of easterly and westerly mean wind differences, respectively.

Between about 120 and 60 hPa the L42 − L72 differences in EP flux divergence show a layered structure in both the NH and SH extratropics, with negative values centered around 85 hPa surrounded by positive values above and below. This may reflect the effects of the abrupt change in vertical resolution in the L42 model to a much coarser grid above ~90 hPa which has no counterpart in the L72 model (which has a constant vertical-level spacing of ~550 m; Fig. 1). Waves with vertical wavelengths smaller than, say, ~2.2 km can be resolved below the ~90-hPa level in both the L42 and L72 models, but cannot be resolved above the ~90-hPa level in the L42 model. The EP flux differences near 90 hPa suggest that the L42 waves are artificially damped and/or reflected near 90 hPa. The effect may also affect the local BDC (Fig. 11g). These results indicate the importance of using a constant, or slowly varying, vertical-level spacing in climate models to avoid

artificial discontinuities in representation of waves and wave–mean flow interaction processes.

The L72 − L168 EP flux difference vectors are downward near 45°N (Fig. 12c) in the region of easterly mean wind differences (Fig. 11e); statistically significant positive EP flux divergence differences are found ~10–20 hPa. Since the vertical resolution (up to 5 hPa) is the same for L72 and L168, this may reflect the effects of the upper branch of the BDC on the middle stratosphere (e.g., Birner and Bönisch 2011). Accurate representation of the full BDC is related to the mean zonal wind structure and is associated with modification of EP flux divergence. The differences between the L42 and L168 models are more distinct (Fig. 12d).

Figure 13 is a map of SLP and precipitation differences for each of L42 − L72, L72 − L168, and L42 − L168. The L42 − L72 differences in the SLP are positive along ~60°N and slightly negative near 40°N; these are associated with the easterly surface wind differences around 50°N and westerly differences near 75°N (Fig. 11d: note surface westerly differences near 75°N are not colored as they are not statistically significant). In the NH, precipitation differences are positive in the midlatitudes and slightly negative in the higher latitudes, opposite in sign to the SLP differences, just as was seen in the L34 − L42 results (Fig. 8). The L72 − L168 differences in both SLP and precipitation are small and occur in conjunction with small differences in tropospheric zonal winds (Fig. 11e). Despite the small magnitude, the signs of the SLP differences in the SH high latitudes are opposite in L42 − L72 (positive) and L72 − L168 (negative) in association with the easterly and westerly anomalies at ~60°S in L42 − L72 and L72 − L168, respectively (Figs. 11d,e). The reason for these small differences is not clear. The L42 − L168 SLP differences in the SH high latitudes are almost negligible.

The NH L42 − L168 differences are more distinct. Enhanced precipitation and lower SLP are found along ~35°N in the L42 model, which is associated with tropospheric subtropical jet modulation (Fig. 11f). These results indicate that both the stratospheric vertical resolution and the inclusion of the upper stratosphere and mesosphere can affect representations of tropospheric phenomena, including the precipitation distribution. More specifically, stratospheric vertical resolution is more important than including the mesosphere as shown by the L42 − L72 versus L72 − L168 comparison.

Next, we investigate the effects of stratospheric vertical resolution on the representation of zonal wind in more detail by comparing L42 with L72. As shown in Fig. 11d, there is a mean easterly bias in L42 relative to L72 in the equatorial stratosphere presumably associated with the absence of a QBO in the L42 version. Holton and Tan (1980) indicate that the stratospheric polar night jet becomes weaker when the QBO is in its easterly phase as extratropical quasi-stationary planetary waves cannot penetrate into the equatorial easterly and are thus more confined to higher latitudes, leading to larger westward wave forcing and a weaker polar night jet.

However, the L42 polar night jet to the north of 60°N is clearly stronger than in the L72 simulation (Fig. 11d), suggesting that the presence or absence of the QBO cannot explain the polar night jet differences in this way; the vertical resolution appears to directly influence the internal dynamics of the polar night jet.

As a test of this issue, the L72 experiment was repeated with a "nudging" of the zonal-mean zonal wind in the tropical stratosphere designed to keep the L72 equatorial winds close to those in the L42 experiment (i.e., to exclude the presence of the QBO in the L72 simulation). Specifically, following Akiyoshi et al. (2009) and Yamashita et al. (2011), the equations in the model were modified by including with an extra momentum relaxation term so that

$$\partial\overline{u}/\partial t = -\tau_x(\overline{u} - \overline{u}_{\text{nudge}}), \tag{1}$$

$$\tau_x = -\frac{1}{\tau}\exp[-(y^2/2y_h^2) - (z - z_0)^2/2z_h^2]. \tag{2}$$

Here, $\overline{u}$ is the L72 zonal-mean zonal wind and $\overline{u}_{\text{nudge}}$ is the L42 climatological annual cycle of monthly mean zonal wind in the equatorial stratosphere. Nudging is performed from 20°N to 20°S and 76 to 4 hPa. The value of τ is set to 5 days; $y_h = 10°$, $z_0 = 27$ km, and $z_h = 8$ km, where y and z are latitude and altitude, respectively. The integration of the nudging experiment was 100 years.

Figure 14a shows latitude–height cross sections of the L42 − L72 zonal-mean zonal wind differences (same as Fig. 11d); Fig. 14b shows the L42 results minus the L72 results with the nudging toward the L42 equatorial zonal wind climatology (referred to as "L72nL42"); Fig. 14c shows the L72nL42 − L72 differences. The zonal wind differences are nearly zero over the stratospheric equatorial regions for L42 − L72nL42 (Fig. 14b), which shows that the nudging largely succeeds in keeping the mean wind close to the L42 climatology, although there are some large L72nL42 − L72 mean zonal wind differences just outside the nudging region.

The extratropical zonal wind anomalies in L42 − L72nL42 (Fig. 14b) are similar in structure to those in L42 − L72 (Fig. 14a). On the other hand, the only significant differences in the L72nL42 − L72 fields are in the equatorial region, with virtually no impact at the high latitudes (Fig. 14c). This result supports the conclusion that it is the higher vertical resolution in L72 that directly

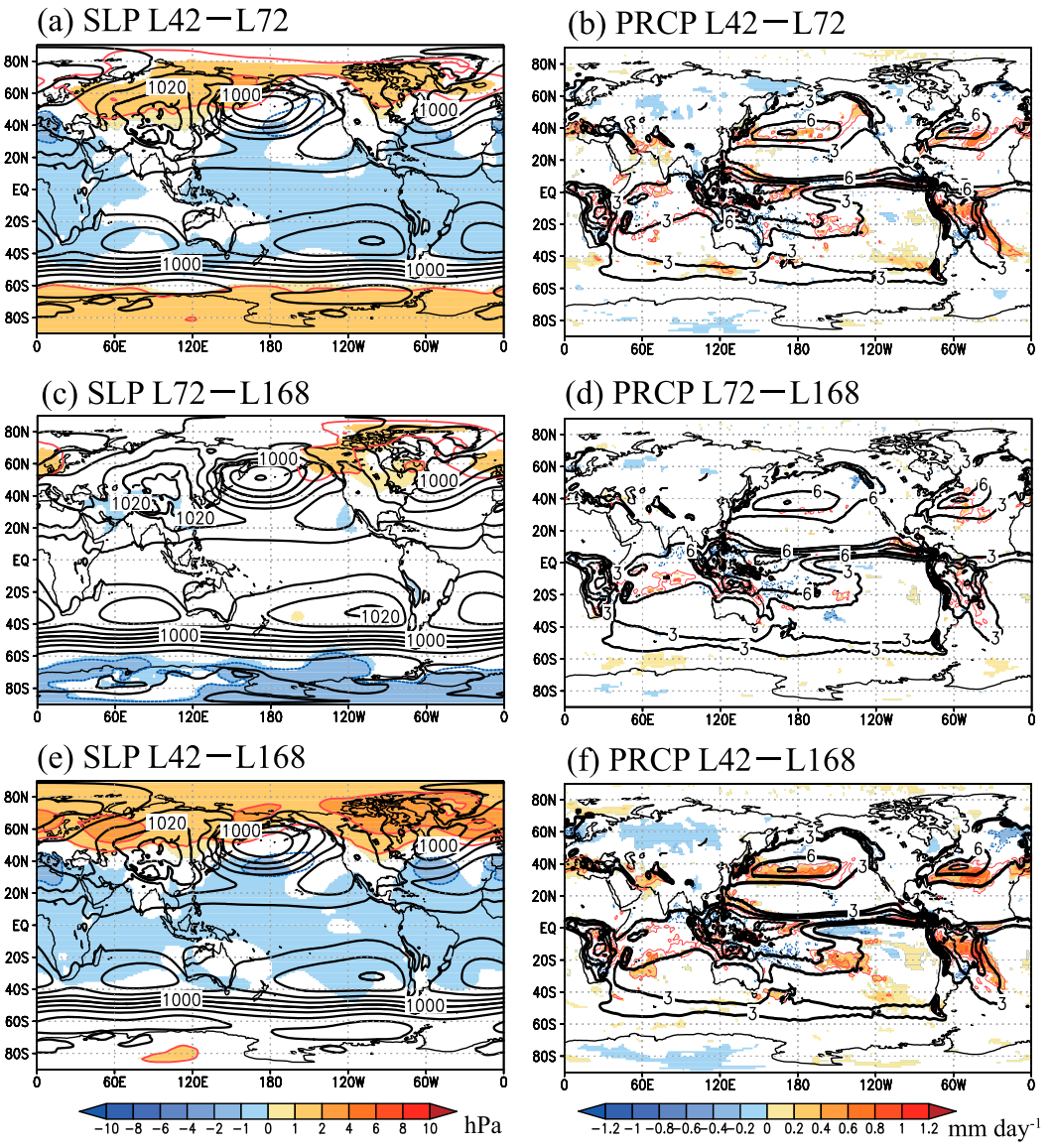

FIG. 13. Horizontal maps of the DJF climatological-mean (left) SLP and (right) precipitation differences for (a),(b) L42 − L72; (c),(d) L72 − L168; and (e),(f) L42 − L168. The black contour lines are the climatological means of SLP and precipitation in (a),(b) L42; (c),(d) L72; and (e),(f) L42 with intervals of 5 hPa and 3 m day^{-1}, respectively. The color shading is at ±1, ±2, ±4, ±6, ±8, and ±10 hPa for SLP, and intervals are 0.2 mm day^{-1} for precipitation. Values with a statistical confidence ≥95% are colored.

improves the climatological polar night jet structure (i.e., equatorward shift and meridional widening of the polar night jet core) and not the presence of the QBO.

6. Effects of a well-resolved stratosphere in other seasons

Up to this point we have focused on phenomena during boreal winter (i.e., DJF). In this section we describe more briefly the impacts of enhanced stratospheric representation on the simulated climate in other seasons.

We begin by presenting some metrics of how well the simulated zonal-mean climatology agrees with the ERA-I (1979–98 mean; see Figs. 2 and 3) in the various model versions considered. Figure 15 shows the root-mean-square errors (RMSEs) of zonal-mean temperature and zonal wind versus ERA-I for the L168, L72, L42, and L34 models for DJF, March–May (MAM), June–August (JJA), and September–November (SON). RMSEs are area and mass weighted. Values are shown for the full globe with vertical averages from 1000 to 85 hPa (the top of L34 without sponge layers) and also

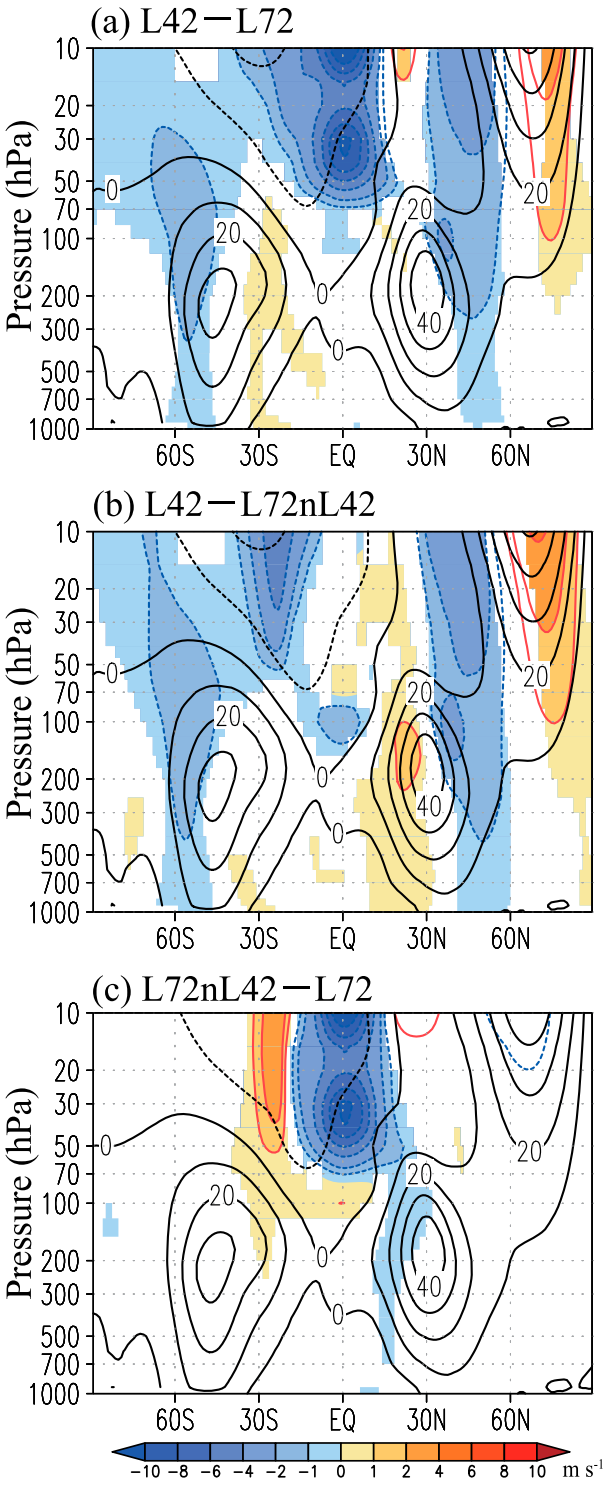

FIG. 14. Latitude–height cross sections of the climatological DJF-mean zonal-mean zonal wind differences for (a) L42 − L72, (b) L42 − L72 nudged with L42 equatorial zonal winds (L72nL42), and (c) L72nL42 − L72. Contour lines show climatological zonal wind from (a),(b) L42 and (c) L72nL42. The color shading is at ±1, ±2, ±4, ±6, ±8, and ±10 m s^{-1}. Values with a statistical confidence ≥95% are colored. Black contour intervals are 10 m s^{-1}.

from 70 to 10 hPa. Also presented in the figure are the RMSEs calculated over just the polar cap regions taken here as 60°–90°N and 60°–90°S.

Global RMSEs of temperature from 1000 to 85 hPa (Fig. 15a) show similar values among L42, L72, and L168 but are larger for L34 in all seasons. As shown in Fig. 2f, there are relatively large cold biases at 85–300 hPa in the high-latitude NH and SH during DJF, resulting from weaker BDC downwelling (Fig. 5b). Similar cold biases are found in NH and SH for MAM, and in SH for JJA and SON (not shown), which result in larger RMSEs in the L34 relative to other model configurations (Figs. 15e,i).

Global RMSEs of zonal-mean zonal wind from 1000 to 85 hPa are quite small (less than 2 m s^{-1}) in each model configuration (Fig. 15b). RMSEs of zonal wind in the L34 depend strongly on season (smallest in DJF and SON, largest in MAM). In DJF, the westerly biases around the subtropical jet are found in the L42, L72, and L168 but they are small in the L34 (Fig. 3). The area of large westerly bias elongates toward the tropical stratosphere around 30–50 hPa which is indicative of a tropical stratospheric long-term mean zonal wind bias in the MIROC model. On the other hand, westerly biases around 200–85 hPa and 60°–80°N are seen only in the L34 associated with cold polar temperature biases (see Figs. 2f, 3f for DJF case). In the polar caps, RMSEs are obviously largest in the L34 model during DJF and MAM for the NH and during MAM and SON in the SH (Figs. 15f,j).

Turning to the stratosphere now, the RMSEs of temperature from 70 to 10 hPa averaged over the globe are always smaller in L168 than in the L42 or L72 results (Fig. 15c). In the DJF and JJA seasons, much larger RMSEs are found in winter polar cap (60°–90°N for DJF and 60°–90°S for JJA), and values in L168 are much smaller than in L42 or L72 (Figs. 15g,k). Most of these RMSEs can be attributed to the cold biases in the polar stratosphere, and as we saw earlier, the polar biases are reduced by including the full stratosphere and mesosphere with higher vertical resolution. In SON, RMSEs in the polar caps are larger in the SH than in the NH, while they are not very different between the NH and SH in MAM.

RMSEs of zonal-mean zonal wind from 70 to 10 hPa averaged over the globe are smaller in L168 than in the L42 or L72 except in SON (Fig. 15d). In both DJF and JJA, the RMSEs computed over the winter polar caps indicate successive improvement in the simulations at L42, L72, and L168 (Figs. 15h,l).

Figure 16 is a Taylor diagram summarizing metrics of the biases in the simulated seasonal zonal-mean climatological temperature and zonal wind when compared with the ERA-I result as reference. Results are presented

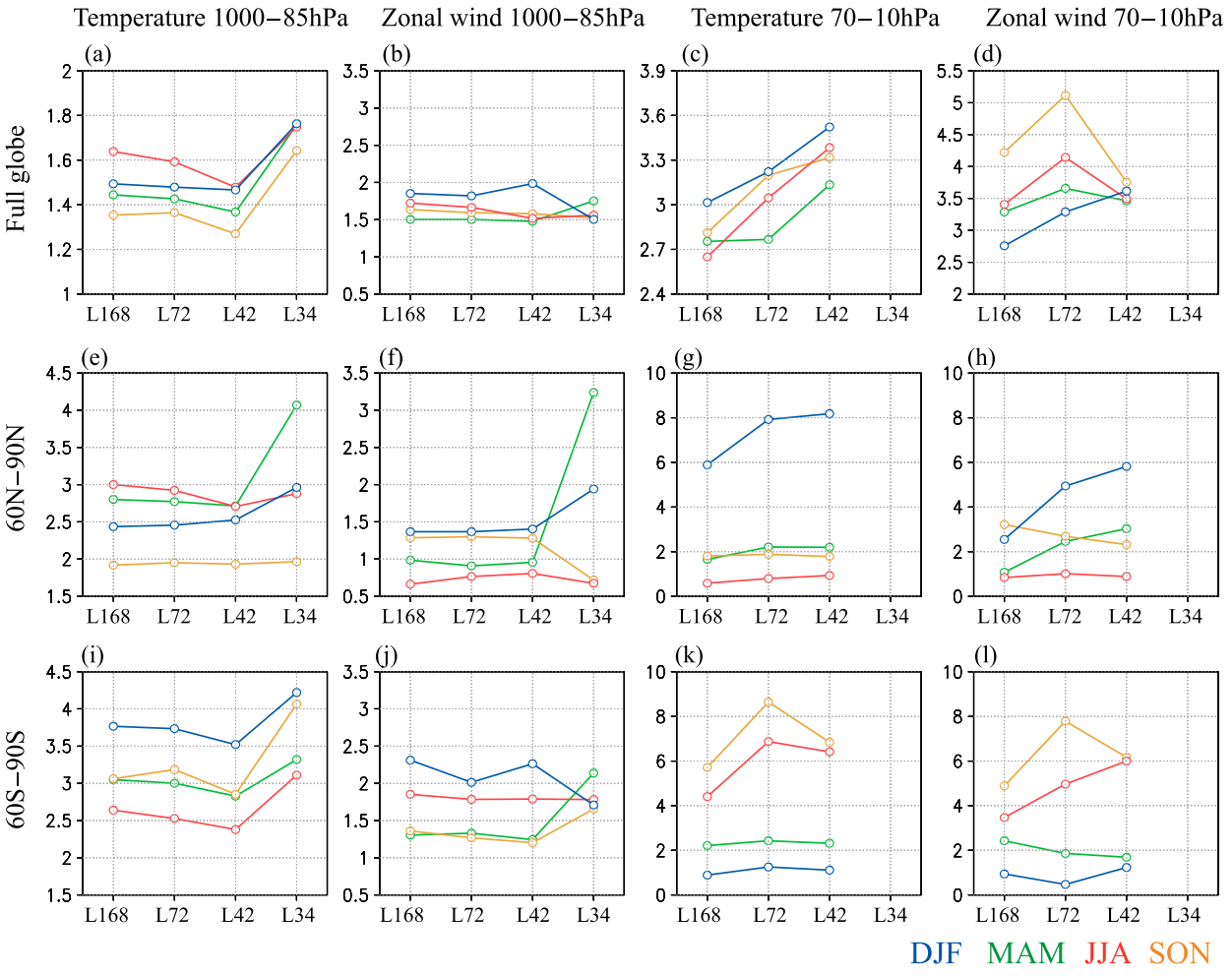

FIG. 15. The RMSEs of zonal-mean (first column),(third column) temperature (K) and (second column),(fourth column) zonal-mean zonal wind ($m\,s^{-1}$) vs ERA-I for the L168, L72, L42, and L34 models for DJF (blue), MAM (green), JJA (red), and SON (yellow) calculated over the height–latitude plane. RMSEs are area and mass weighted. Results are shown (a)–(d) for the full globe, and for polar caps bounded by (e)–(h) 60°–90°N and (i)–(l) 60°–90°S, with a vertical range from 1000 to 85 hPa for the first and second columns and from 70 to 10 hPa for the third and fourth columns. RMSEs of 70–10 hPa are missing for L34.

for the four model configurations with the metrics calculated over the same domains as used in Fig. 15. The standard deviation in each case is normalized by the ERA-I value and the correlation is plotted as the cosine of the angle from the horizontal axis. Note that the distances between the reference point (ERA-I; black circle in Fig. 16) and each model correspond to the centered RMS difference (i.e., biases of the mean fields are subtracted, in contrast to the RMSEs quoted in Fig. 15 which include the mean biases over the whole height–latitude region considered in each case).

The spatial correlations of the full globe average (Figs. 16a–d) are all quite large and the model standard deviations are close to that of ERA-I over the height–latitude plane, so the points in the Taylor diagram for the model all cluster very close to the observed reference point. In contrast, the diagrams for the polar caps show some scatter.

At 1000–85 hPa in the polar caps, the metrics of zonal wind simulated climatology in L34 are much worse compared with L42, L72, and L168 during DJF and MAM in the NH, when the RMSEs are also large (Fig. 15f), suggesting that models including a stratosphere could improve representation of the zonal-mean zonal wind at 1000–85 hPa. The RMSE values and Taylor diagrams for SLP and 850-hPa geopotential height in polar caps also show better agreement to ERA-I in L42, L72, and L168 than in L34 (not shown). RMSE differences also reveal that the simulated precipitation climatology is closer to observations in L42, L72, and L168 than in L34 (not shown). Note, however, that all these metrics of the quality of the model simulation will depend significantly

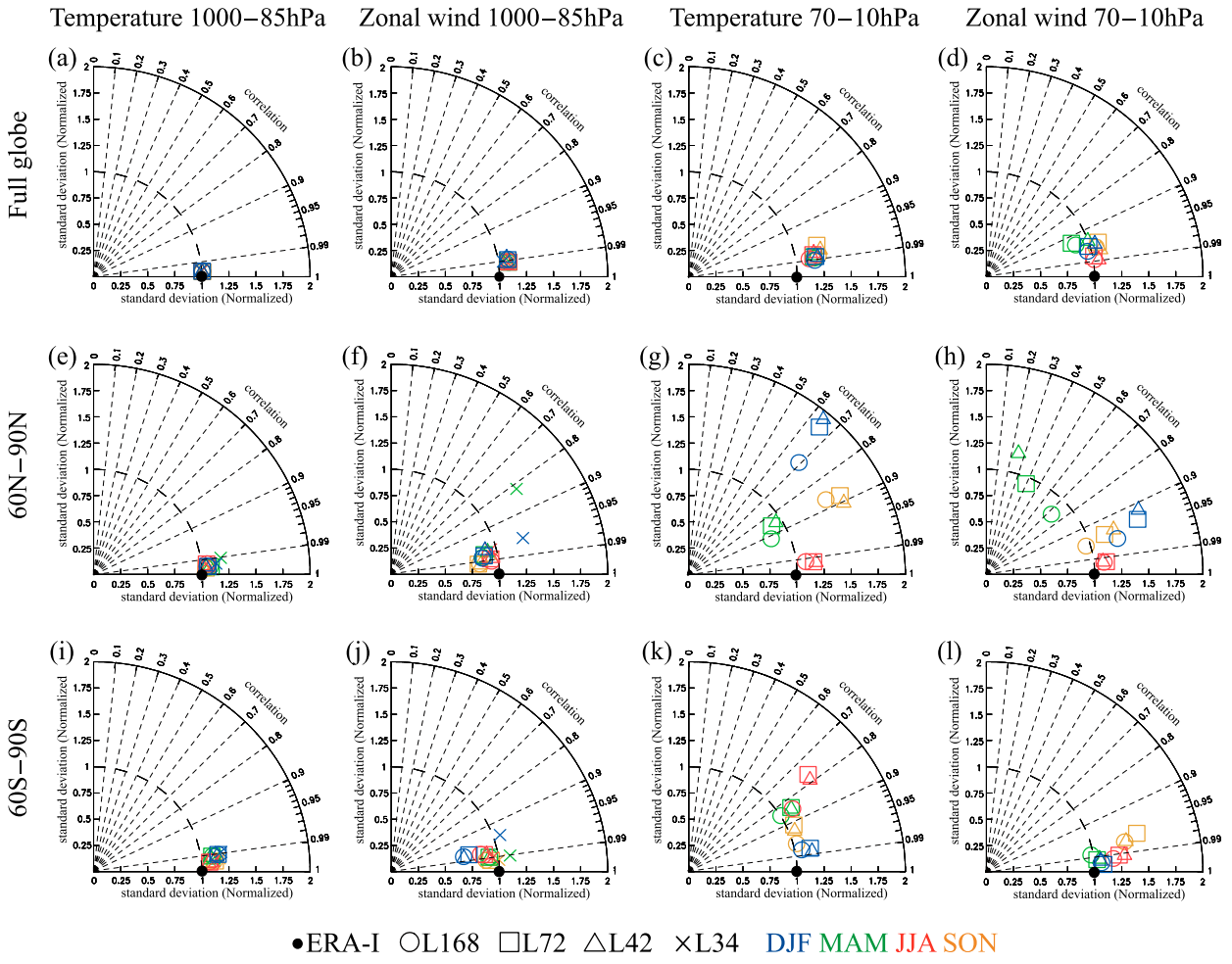

FIG. 16. Taylor diagrams showing the differences between simulated seasonal-mean, zonal-mean climatology and the reference climatology based on ERA-I. Results are shown for the four model configurations calculated over the height–latitude plane in (first column),(third column) zonal-mean temperature and (second column),(fourth column) zonal-mean zonal wind. Results are shown (a)–(d) for the full globe, and for polar caps bounded by (e)–(h) 60°–90°N and (i)–(l) 60°–90°S, with vertical ranges from 1000 to 85 hPa for the first and second columns and from 70 to 10 hPa for the third and fourth columns. The standard deviation is normalized by ERA-I (black dot). Open circles, squares, triangles, and crosses represent the L168, L72, L42 and L34 models, respectively. Blue, green, red, and yellow colors show DJF, MAM, JJA and SON, respectively. Values in 70–10 hPa are not shown for the L34.

on the parameterizations of moist convection, surface drag, and topographic gravity wave effects.

In the NH polar cap at 70–10 hPa (Figs. 16g,h), metrics of both zonal-mean temperature and zonal wind fields are improved successively in L42, L72, and L168, especially during winter. The lowest correlation of zonal wind is found in MAM (~0.25 for L42) when simulated westerlies in the polar stratosphere are much larger than in ERA-I (not shown), possibly resulting from a bias in the timing of final stratospheric warmings in the simulations. However, this deficiency is improved successively in L42, L72, and L168 (L168 correlation is ~0.72). In the SH polar cap (Figs. 16k,l), scores do not scatter among models/seasons as much as in the NH, but improvement in the simulated climatology by using more vertical levels is also apparent, especially in JJA temperature. Overall the metrics presented in Figs. 15 and 16 support our contention that including a well-resolved stratosphere generally improves the zonal-mean temperature and zonal wind fields in all seasons.

We now examine the spatial distributions of zonal-mean temperature, zonal wind, and residual-mean vertical velocity differences for L34 − L42 during MAM, JJA, and SON (Fig. 17). Structures of temperature differences in MAM, JJA, and SON are similar to those in DJF (Fig. 4a), showing warmer temperatures at lower latitudes in the L34 version compared with L42, and colder temperatures at higher latitudes above ~300 hPa.

The zonal-mean zonal wind differences also show similar distributions among seasons with statistically

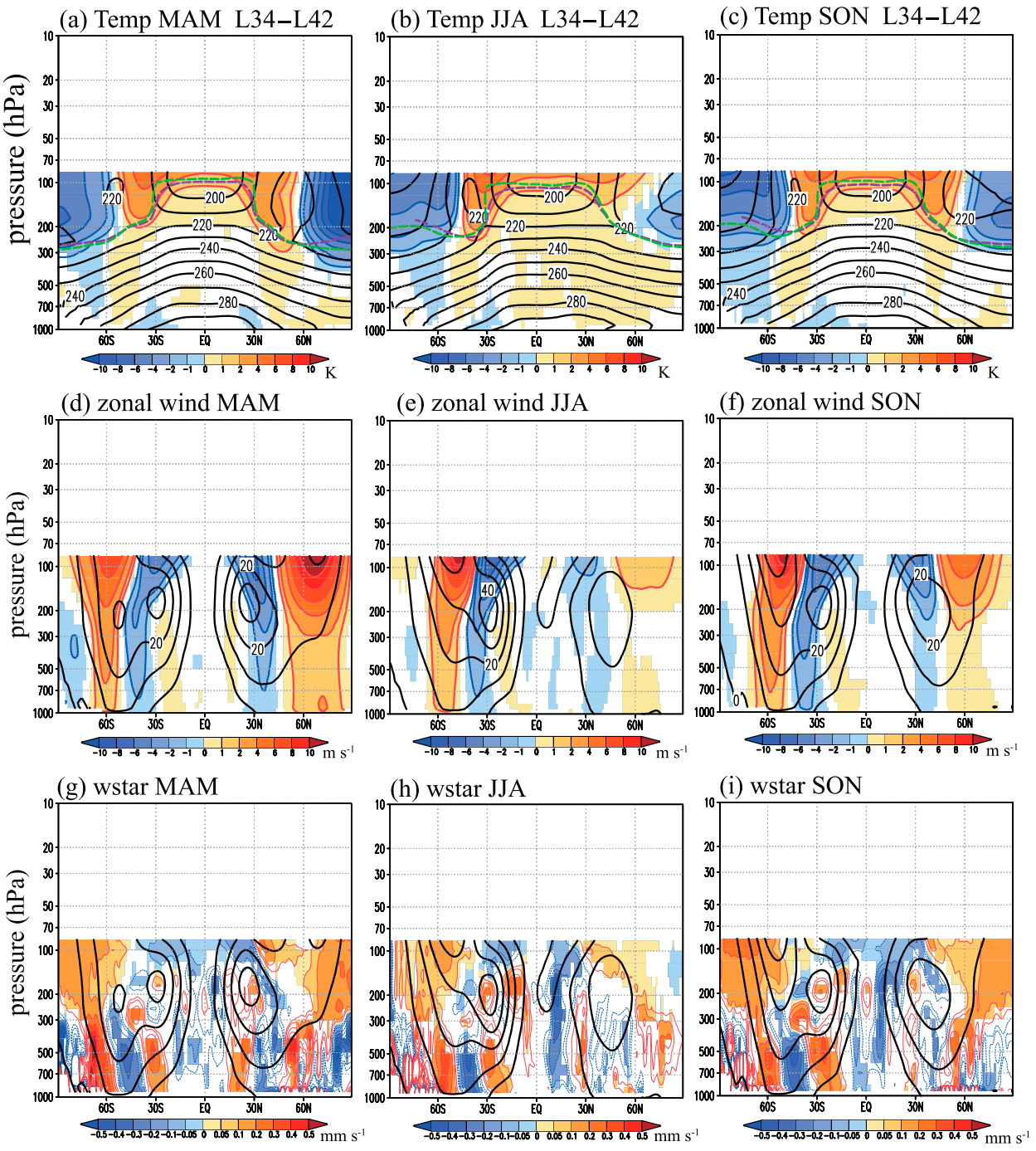

FIG. 17. As in Fig. 11, but for latitude–height cross sections of the climatological (left) MAM-mean, (center) JJA-mean, and (right) SON-mean (a)–(c) zonal-mean temperature, (d)–(f) zonal-mean zonal wind, and (g)–(i) residual-mean vertical velocity differences for L34 − L42. Solid contour lines show L34 climatological variables. The dashed lines in (a)–(c) show tropopause heights for L34 (purple) and L42 (green). The L34 tropical tropopause by the World Meteorological Organization definition is not clear at 70°–90°S in JJA and SON.

significant westerly anomalies extending from the lower stratosphere to the surface in high latitudes. Positive anomalies of the residual vertical velocity are also found in higher latitudes, corresponding to weaker downwelling in the L34 version (see Fig. 5b for DJF). Note that the BDC in higher-latitudes lower stratosphere shows downwelling in all seasons and hemispheres and the seasonal and interhemispheric

differences are less pronounced than in the middle and upper stratosphere (see Fig. 5 in Butchart 2014). Therefore differences of the residual vertical velocity between L34 and L42 may not have a pronounced seasonal and interhemispheric dependence. As a consequence the pattern of wind and temperature biases seen in the L34 minus L42 differences in temperature and zonal wind are somewhat similar among seasons.

We have also investigated for the other seasons the differences in latitude–height cross sections of zonal-mean eddy meridional flux of zonal momentum and heat flux, 850-hPa zonal wind, and eddy heat flux and SAT, SLP, and precipitation (corresponding to Figs. 6–8). They are all qualitatively similar to those in DJF, although some quantitative differences are found among seasons (not shown). Overall the schematic illustration of Fig. 10 in DJF could apply to the both hemispheres for all seasons.

The same differences, but for L42 − L168, are shown in Fig. 18 (see Figs. 11c,f,i for DJF). In JJA (center panels), colder temperatures are found in the SH polar stratosphere at L42 and warmer temperatures are seen in the NH, where residual vertical velocity anomalies are positive and negative, respectively. These difference patterns in stratospheric higher latitudes are similar, but of opposite sign, to those in DJF. Westerly anomalies on the polar side and easterly anomalies in the equatorward side of the polar night jet are also similar to those in DJF. In MAM and SON, cold temperature anomalies and westerly anomalies in the stratospheric polar regions are seen in both the NH and the SH, associated with positive residual vertical velocity anomalies (although NH positive anomalies we computed in MAM are not statistically significant).

7. Summary and concluding remarks

This paper reports on an investigation of the effects of including a well-resolved stratosphere (and mesosphere) in the global atmospheric MIROC-AGCM climate model. The analysis focused primarily on the NH winter circulation, including the SLP and precipitation fields. The investigation examined the modeled climate from four different configurations with model tops at ~27 km (L34), 47 km (L42), 47 km (L72), and 100 km (L168). The four configurations had identical horizontal resolution (T106) and identical vertical-level structures in the troposphere (more precisely up to ~90 hPa), as well as identical physical subgrid-scale parameterizations. Each model configuration was run for 100 years in simulations with annually repeating prescribed SSTs and ozone concentrations.

Overall the circulation in the L168 model is most realistic and successive degradations of the vertical grid to the L72, L42, and L34 configurations result in progressively less realistic simulations. In the tropical stratosphere the dependence on vertical resolution is shown most dramatically with the L168 and L72 versions simulating a fairly realistic QBO, while the L42 version had weak easterly zonal winds at most heights with almost no interannual variability. This strong dependence of the simulated tropical stratospheric mean winds on the vertical resolution is familiar from other global models (e.g., Hamilton et al. 1999) and likely results from the contributions of rather short vertical-scale waves to the QBO.

The L42 − L72 comparison illustrates the impact of vertical resolution in the stratosphere. The differences in EP flux divergence show a layered structure in both the NH and SH extratropics between 120 and 60 hPa, a region where an abrupt vertical-resolution change occurs in the L42 but there is constant level spacing in the L72 model (Fig. 1). This underlines the importance of constant, or slowly varying, vertical-level spacing in climate models to avoid artificial discontinuities in representation of waves and wave–mean flow interaction processes.

In the NH winter stratosphere even the T106L168 model displays a cold-pole bias relative to observations, but successive degradations of the vertical-level structure to L72, L42, and L34 led to a worsening cold pole bias. As the cold pole bias becomes more severe, the simulated polar night jet becomes stronger and less realistic. The magnitude of the winter cold pole bias is negatively correlated with the strength of the simulated mean downwelling—and adiabatic heating—at high latitudes. The analysis indicates that a lower model top and reduced vertical resolution in the stratosphere both lead to suppression of the BDC and so to stratospheric winter polar temperatures that are closer to radiative equilibrium.

The effects of the reduced polar downwelling in degraded vertical grid configurations extend into the troposphere and affect even the circulation at the surface. The sense of this is that the stronger mean westerlies in the lower stratosphere in simulations with a poorly resolved stratosphere (L34) are connected with tropospheric circulations with a more positive AO phase. This confirms the results from previous studies that have indicated that low-top models simulate lower polar SLP than do high-top models (e.g., Sassi et al. 2010). The present study extends this result to describe how the stratosphere affects surface temperature and precipitation distributions in association with these changes in SLP and zonal winds.

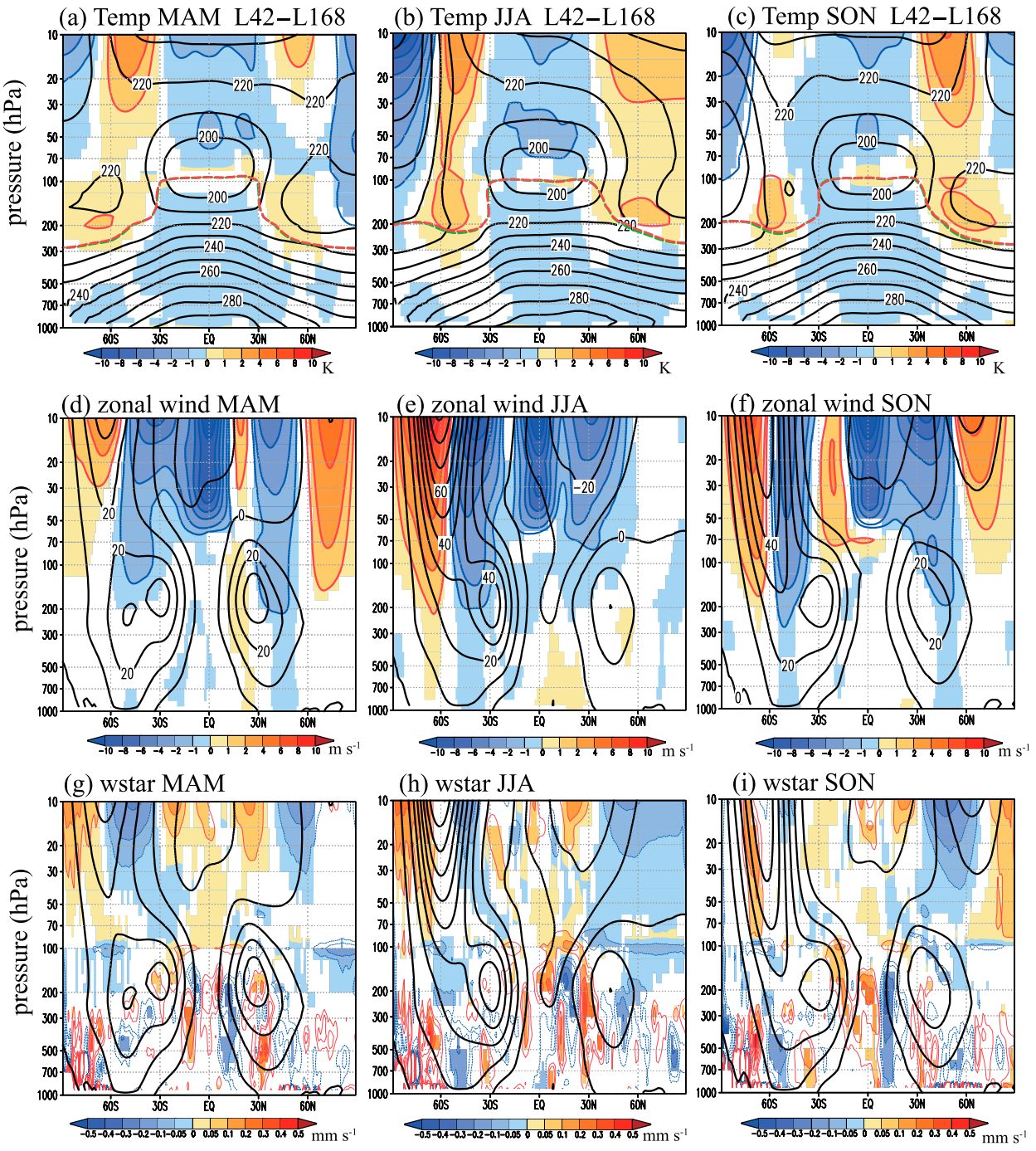

FIG. 18. As in Fig. 17, but for L42 − L168. Solid contour lines show L42 climatological variables. The dashed lines in (a)–(c) show tropopause heights for L42 (green) and L168 (red), which are nearly identical.

In the present paper we have mainly discussed the DJF mean, but climatology differences of the zonal wind, temperature, and residual vertical velocity in L34 − L42 are qualitatively similar among the seasons.

We also explicitly demonstrated that the vertical resolution in the stratosphere (L42 − L72) is of greater importance than the inclusion of a mesosphere (L72 − L168) when considering the impact on the troposphere. Note the overall connection between stratospheric vortex strength and tropospheric AO anomalies introduced by degrading the stratospheric representation is also characteristic of the observed NH natural

variability over a wide range of time scales (Kidston et al. 2015).

We should note here that even a low-top model can simulate a realistic strength of the polar night jet through the addition of artificial zonal forcing (e.g., Rayleigh friction) applied to the zonal-mean components of the circulation or by including an appropriately tuned parameterization of the effects of nonstationary subgrid-scale gravity waves. Such approaches have limitations when applied to climate change studies as there may be no convincing way to adjust the extra forcing (e.g., Rayleigh friction coefficient or wave sources in a gravity wave parameterization) to account for the changed climate. This is a concern as the stratospheric BDC is expected to change significantly as part of the global warming response of the atmosphere to increased greenhouse gas forcing (e.g., Kawatani and Hamilton 2013; Butchart 2014). The present study investigated the effects of the representation of the stratosphere in global models formulated without imposing additional angular momentum sources.

Modifications of tropospheric circulation associated with ocean–atmosphere coupling processes were not represented in the present experiments. It would be interesting to perform similar high-top and low-top experiments using coupled atmosphere–ocean global models to investigate ocean–troposphere–stratosphere–mesosphere coupling. This remains a subject for future investigation. In the same vein the present study used prescribed ozone concentrations and so ignored an important coupling between dynamics and stratospheric chemistry. It may be interesting to repeat our experiments with a coupled dynamics–chemistry model.

Here we have used the results of our systematic experiments to document the limitations introduced by inadequate resolution of the stratosphere in global atmospheric models. This sensitivity study has shown that improved stratospheric representation in MIROC-AGCM reduces the prominent AO+-type biases extending down to the lower troposphere seen in our MIROC simulations in a very low-top model configuration (i.e., L34). Thus, we can expect that for models that display an AO+-type bias in the troposphere the basic simulation may be improved by inclusion of a more complete representation of the stratosphere. Our results, as well as those in earlier studies (e.g., Scaife et al. 2012), show that stratosphere–troposphere interactions are important and an accurate and physically correct simulation of surface climate requires a well-resolved stratosphere, so the value of this kind of study is to provide a road map for objective evaluation of the impact of this improvement in the context of model optimization.

Acknowledgments. We express our gratitude to two anonymous reviewers for their valuable comments on the original manuscript. We also thank Professors Y. N. Takayabu and H. Nakamura and Drs. T. Horinouchi and Y. Kosaka. YK was supported by Japan Society for Promotion of Science (JPSP) KAKENHI Grants JP15KK0178, JP15H02132, JP17K18816, and JP18H01286 and by the Environment Research and Technology Development Fund (2-1503) of Environmental Restoration and Conservation Agency, Japan. YK and KH were also supported by the Japan Agency for Marine-Earth Science and Technology (JAMSTEC) through its sponsorship of research at the International Pacific Research Center. This is IPRC Publication Number 1364. YY was supported by JSPS KAKENHI Grant JP16K16186. This study was partly supported by the Japan Science and Technology Agency (JST) as part of the Belmont Forum. LG and SO acknowledge funding from the U.K. Natural Environment Research Council (NERC) through support of the Atlantic Climate System Integrated Study (ACSIS) Programme of the National Centre for Atmospheric Science (NCAS) and the Belmont Grant NE/P006779/1–GOTHAM–1505DC004/MW2. The numerical simulations in this study were performed using the Earth Simulator. The GFD-Dennou library and GrADS were used to draw the figures.

REFERENCES

Akiyoshi, H., and Coauthors, 2009: A CCM simulation of the breakup of the Antarctic polar vortex in the years 1980–2004 under the CCMVal scenarios. *J. Geophys. Res.*, **114**, D03103, https://doi.org/10.1029/2007JD009261.

Baldwin, M. P., and T. J. Dunkerton, 2001: Stratospheric harbingers of anomalous weather regimes. *Science*, **294**, 581–584, https://doi.org/10.1126/science.1063315.

Birner, T., and H. Bönisch, 2011: Residual circulation trajectories and transit times into the extratropical lowermost stratosphere. *Atmos. Chem. Phys.*, **11**, 817–827, https://doi.org/10.5194/acp-11-817-2011.

Boville, B. A., and X. Cheng, 1988: Upper boundary effects in a general circulation model. *J. Atmos. Sci.*, **45**, 2591–2606, https://doi.org/10.1175/1520-0469(1988)045<2591:UBEIAG>2.0.CO;2.

Butchart, N., 2014: The Brewer-Dobson circulation. *Rev. Geophys.*, **52**, 157–184, https://doi.org/10.1002/2013RG000448.

Charlton-Perez, A. J., and Coauthors, 2013: On the lack of stratospheric dynamical variability in low-top versions of the CMIP5 models. *J. Geophys. Res. Atmos.*, **118**, 2494–2505, https://doi.org/10.1002/jgrd.50125.

Dee, D. P., and Coauthors, 2011: The ERA-Interim reanalysis: Configuration and performance of the data assimilation system. *Quart. J. Roy. Meteor. Soc.*, **137**, 553–597, https://doi.org/10.1002/qj.828.

Gray, L. J., J. A. Anstey, Y. Kawatani, H. Lu, S. Osprey, and V. Schenzinger, 2018: Surface impacts of the quasi biennial oscillation. *Atmos. Chem. Phys.*, **18**, 8227–8247, https://doi.org/10.5194/acp-18-8227-2018.

Hamilton, K., R. J. Wilson, and R. Hemler, 1999: Middle atmosphere simulated with high vertical and horizontal resolution

versions of a GCM: Improvement in the cold pole bias and generation of a QBO-like oscillation in the tropics. *J. Atmos. Sci.*, **56**, 3829–3846, https://doi.org/10.1175/1520-0469(1999)056<3829:MASWHV>2.0.CO;2.

Hardiman, S. C., N. Butchart, T. J. Hinton, S. M. Osprey, and L. J. Gray, 2012: The effects of a well-resolved stratosphere on surface climate: Differences between CMIP5 simulations with high and low top versions of the Met Office climate model. *J. Climate*, **25**, 7083–7099, https://doi.org/10.1175/JCLI-D-11-00579.1.

Hasumi, H., and S. Emori, 2004: K-1 coupled GCM (MIROC) description. University of Tokyo Center for Climate System Research Tech. Rep., 34 pp., http://ccsr.aori.u-tokyo.ac.jp/~hasumi/miroc_description.pdf.

Haynes, P. H., M. E. McIntyre, T. G. Shepherd, C. J. Marks, and K. P. Shine, 1991: On the "downward control" of extratropical diabatic circulations by eddy-induced mean zonal forces. *J. Atmos. Sci.*, **48**, 651–678, https://doi.org/10.1175/1520-0469(1991)048<0651:OTCOED>2.0.CO;2.

Holton, J. R., and H.-C. Tan, 1980: The influence of the equatorial quasi-biennial oscillation on global circulation at 50 mb. *J. Atmos. Sci.*, **37**, 2200–2208, https://doi.org/10.1175/1520-0469(1980)037<2200:TIOTEQ>2.0.CO;2.

Kawatani, Y., and K. Hamilton, 2013: Weakened stratospheric quasibiennial oscillation driven by increased tropical mean upwelling. *Nature*, **497**, 478–481, https://doi.org/10.1038/nature12140.

——, M. Takahashi, K. Sato, S. P. Alexander, and T. Tsuda, 2009: Global distribution of atmospheric waves in the equatorial upper troposphere and lower stratosphere: AGCM simulation of sources and propagation. *J. Geophys. Res.*, **114**, D01102, https://doi.org/10.1029/2008JD010374.

——, K. Hamilton, and S. Watanabe, 2011: The quasi-biennial oscillation in a double CO_2 climate. *J. Atmos. Sci.*, **68**, 265–283, https://doi.org/10.1175/2010JAS3623.1.

——, J. N. Lee, and K. Hamilton, 2014: Interannual variations of stratospheric water vapor in MLS observations and climate model simulations. *J. Atmos. Sci.*, **71**, 4072–4085, https://doi.org/10.1175/JAS-D-14-0164.1.

Kidston, J., A. A. Scaife, S. C. Hardiman, D. M. Mitchell, N. Butchart, M. P. Baldwin, and L. J. Gray, 2015: Stratospheric influence on tropospheric jet streams, storm tracks and surface weather. *Nat. Geosci.*, **8**, 433–440, https://doi.org/10.1038/ngeo2424.

Kodera, K., B. M. Funatsu, C. Claud, and N. Eguchi, 2015: The role of convective overshooting clouds in tropical stratosphere–troposphere dynamical coupling. *Atmos. Chem. Phys.*, **15**, 6767–6774, https://doi.org/10.5194/acp-15-6767-2015.

Li, D., and K. P. Shine, 1999: UK Universities Global Atmospheric Modelling Programme (UGAMP) Global Ozone Climatology Project dataset. British Atmospheric Data Centre, accessed 2 June 2018, http://badc.nerc.ac.uk/data/ugamp-o3-climatology/.

Liess, S., and M. A. Geller, 2012: On the relationship between the QBO and distribution of tropical deep convection. *J. Geophys. Res.*, **117**, D03108, https://doi.org/10.1029/2011JD016317.

Lindzen, R. S., E. S. Batten, and J.-W. Kim, 1968: Oscillations in atmospheres with tops. *Mon. Wea. Rev.*, **96**, 133–140, https://doi.org/10.1175/1520-0493(1968)096<0133:OIAWT>2.0.CO;2.

Manzini, E., and Coauthors, 2014: Northern winter climate change: Assessment of uncertainty in CMIP5 projections related to stratosphere-troposphere coupling. *J. Geophys. Res. Atmos.*, **119**, 7979–7998, https://doi.org/10.1002/2013JD021403.

McFarlane, N. A., 1987: The effect of orographically excited gravity wave drag on the general circulation of the lower stratosphere and troposphere. *J. Atmos. Sci.*, **44**, 1775–1800, https://doi.org/10.1175/1520-0469(1987)044<1775:TEOOEG>2.0.CO;2.

Osprey, S. M., L. J. Gray, S. C. Hardiman, N. Butchart, and T. J. Hinton, 2013: Stratospheric variability in twentieth-century CMIP5 simulations of the Met Office climate model: High top versus low top. *J. Climate*, **26**, 1595–1606, https://doi.org/10.1175/JCLI-D-12-00147.1.

Plumb, R. A., and R. C. Bell, 1982: A model of the quasi-biennial oscillation on an equatorial beta-plane. *Quart. J. Roy. Meteor. Soc.*, **108**, 335–352, https://doi.org/10.1002/qj.49710845604.

Sassi, F., R. R. Garcia, D. Marsh, and K. W. Hoppel, 2010: The role of the middle atmosphere in simulations of the troposphere during Northern Hemisphere winter: Differences between high- and low-top models. *J. Atmos. Sci.*, **67**, 3048–3064, https://doi.org/10.1175/2010JAS3255.1.

Scaife, A. A., and Coauthors, 2012: Climate change projections and stratosphere–troposphere interaction. *Climate Dyn.*, **38**, https://doi.org/10.1007/s00382-011-1080-7.

Shepherd, K., K. Semeniuk, and J. N. Koshyk, 1996: Sponge layer feedbacks in middle-atmosphere models. *J. Geophys. Res.*, **101**, 23 447–23 464, https://doi.org/10.1029/96JD01994.

Sigmond, M., J. F. Scinocca, and P. J. Kushner, 2008: Impact of the stratosphere on tropospheric climate change. *Geophys. Res. Lett.*, **35**, L12706, https://doi.org/10.1029/2008GL033573.

Wallace, J. M., and D. S. Gutzler, 1981: Teleconnections in the geopotential height field during the Northern Hemisphere winter. *Mon. Wea. Rev.*, **109**, 784–804, https://doi.org/10.1175/1520-0493(1981)109<0784:TITGHF>2.0.CO;2.

Watanabe, S., H. Miura, M. Sekiguchi, T. Nagashima, K. Sudo, S. Emori, and M. Kawamiya, 2008: Development of an atmospheric general circulation model for integrated Earth system modeling on the Earth Simulator. *J. Earth Simul.*, **9**, 27–35.

Yamashita, Y., H. Akiyoshi, and M. Takahashi, 2011: Dynamical response in the Northern Hemisphere midlatitude and high-latitude winter to the QBO simulated by CCSR/NIES CCM. *J. Geophys. Res.*, **116**, DO6118, https://doi.org/10.1029/2010JD015016.

Yoo, C., and S.-W. Son, 2016: Modulation of the boreal wintertime Madden-Julian oscillation by the stratospheric quasi-biennial oscillation. *Geophys. Res. Lett.*, **43**, 1392–1398, https://doi.org/10.1002/2016GL067762.